Asian Journal of Chemistry; Vol. 37, No. 6 (2025), 1518-1534

ASIAN JOURNAL OF CHEMISTRY

https://doi.org/10.14233/ajchem.2025.33504

Alzheimer's Dementia Targeting by Plant-Derived 2,6-Dimethoxybenzoic Acid: *In vitro*, DFT and Molecular Docking Study

E. EUNICE and JOHANAN CHRISTIAN PRASANA*

Department of Physics, Madras Christian College (Affiliated to University of Madras), East Tambaram-600059, India

*Corresponding author: E-mail: reachjcp@gmail.com

Received: 12 February 2025; *Accepted*: 26 May 2025; *Published online*: 27 May 2025; AJC-22026

2,6-Dimethoxybenzoic acid (2,6-DMBA), a phytochemical from golden eye grass, shows promising therapeutic agent for Alzheimer's dementia (AD). Density functional theory (DFT) calculations with the B3LYP functional and 6-311++G(d,p) basis set were used for the structural optimization, spectroscopic, electronic, topological and biological evaluation. Spectroscopic methods, such as Fourier transform infrared (FT-IR) and Fourier transform raman (FT-Raman) spectroscopy, supported the geometric structure. Topological analyses, including molecular electrostatic potential (MEP), electron localization function (ELF), localized orbital locator (LOL) and reduced density gradient (RDG), identified reactive sites, while natural bond orbital (NBO), natural population analysis (NPA) and Mulliken population analysis (MPA) provided insights into charge distribution, inter- and intramolecular interactions. Nonlinear optical (NLO) properties, Frontier molecular orbital (FMO) analysis, ultraviolet-visible (UV-Vis) spectroscopy and drug-likeness evaluations highlighted its electronic characteristics and potential pharmacokinetic profile. Molecular docking studies revealed strong binding affinities with AD targets β-secretase 1 (BACE-1, 6EQM) and acetylcholinesterase (AChE, 2C5G), suggesting dual inhibitory potential. *In vitro* assay and absorption, distribution, metabolism, excretion and toxicity (ADMET) profiling indicated good oral bioavailability, blood brain barrier (BBB) permeability, low toxicity and favourable pharmacokinetics, supporting that 2,6-DMBA may be a potent compound for developing AD therapeutics.

Keywords: Golden eye grass, DFT, Alzheimer's dementia, Blood brain barrier permeability, Molecular docking, Cytotoxicity.

INTRODUCTION

Alzheimer's dementia (AD) is the most prevalent form of dementia worldwide, posing significant societal and healthcare burdens. This disease is marked by the buildup of amyloid-beta (Aβ) plaques and neurofibrillary tangles, resulting from hyperphosphorylated tau protein, neuroinflammation, oxidative stress and synaptic dysfunction. Although research continues, existing therapies only manage symptoms and do not prevent disease progression [1]. Among various biochemically significant compounds, 2,6-dimethoxybenzoic acid (2,6-DMBA) is a promising candidate for AD. 2,6-Dimethoxybenzoic acid is derived from the *Curculigo orchioides*, often referred to as "Golden eye grass," belonging to the Amaryllidaceae family [2]. This compound has a rich ethnomedical tradition and represents a significant source of phytochemicals with potential medicinal applications [3]. Its known benefits include anti-inflammatory, antioxidant, anticonvulsant, antidepressant and supportive for clotting and neuroprotective functions [4]. 2,6-DMBA appears as a crystalline solid ranging from white to pale yellow, with the pale-yellow colour attributed to methoxy substituents. The title compound features two methoxy groups linked to a benzoic acid backbone, which is vital for biological functions. These methoxy groups enhance radical-scavenging ability at the 2- and 6-positions on the benzoic acid core, thereby protecting neurons from the oxidative stress [5]. Early studies suggest it may lessen oxidative damage and neuroinflammation, both key contributors to AD pathology [6].

2,6-DMBA can act as a weak acid buffer in the biological systems, helping to stabilize cellular pH by neutralizing excess protons in slightly acidic conditions. The pK_a of 2,6-DMBA was found to be 4.73 based on its dissociation constant (K_a = 1.9×10^{-5}) [7], which means that when the concentration of 2,6-DMBA and its conjugate base are in balance, the pH of the

system will stabilize around 4.73, which is beneficial for maintaining the optimal pH for enzyme activity, neurotransmitter function and overall cellular health, particularly in sensitive environments like brain [8]. The mild acidity and buffering capacity of 2,6-DMBA are similar to the natural buffering systems in human blood, which helps maintain a stable pH around 7.4. Due to this pH stability and its ability to act as a mild acid buffer, based on its natural origin, 2,6-DMBA is considered non-hazardous and well-suited for long-term therapeutic use [9].

First-principles simulations (DFT) were used to further investigate the therapeutic potential of 2,6-DMBA by examining its electronic structure, reactivity and molecular interactions with AD-related target proteins, such as BACE-1 and AChE. Computational models indicate that 2,6-DMBA may inhibit amyloid-β aggregation, an essential factor in AD development [10]. Docking studies analyzed its binding strength against commercially available AD medications. Furthermore, its favourable physico-chemical and pharmacokinetic properties, including suitable lipophilicity, pK_a and BBB permeability, support its potential as a drug-like molecule, making it a promising candidate for further investigation.

A comprehensive literature review indicates that no DFT and molecular docking studies have been performed on 2,6-DMBA. Integrating the computational and experimental methods allows for a thorough evaluation of pharmacokinetics and potential efficacy. Among computational approaches, DFT is vital for accurately predicting molecular properties and reactivity, providing key theoretical insights that complement experimental data. To balance computational accuracy with efficiency, the widely used B3LYP functional combined with the 6-311++G (d,p) basis set was selected. This basis set includes diffuse and polarization functions that are essential for accurately describing electron distribution in molecules containing heteroatoms and functional groups such as the methoxy and carboxyl groups present in 2,6-DMBA. Diffuse functions play a crucial role in capturing weak non-covalent interactions like hydrogen bonding and van der Waals forces, which are critical for drug-target binding and molecular recognition. The polarization functions improve the flexibility of electron clouds, leading to more accurate molecular geometries and electronic properties. This level of theory offers a practical balance between computational cost and precision, making it ideal for simulating biologically relevant molecules and their interactions with AD target proteins. Overall, these *in silico* methods complement experimental research by reducing development time and costs and accelerating the discovery of novel multitargeted therapeutics for Alzheimer's dementia and related neurological disorders [11,12].

EXPERIMENTAL

Experimental characterization: 2,6-Dimethoxybenzoic acid was purchased from Evolution Life Sciences (Sigma Aldrich), Chennai, India, with a purity of 98%. FT-IR and FT-Raman spectra were obtained in IIT Madras, SAIF, Chennai, India. FT-IR (4000-400 cm^{-1}) and FT-Raman spectra (4000-100 cm^{-1}) were recorded using KBr method. The cytotoxicity of L929 fibroblast cells was evaluated using an MTT assay at Pondicherry Centre for Biological Science and Educational Trust, Pondicherry, India.

Computational details: DFT calculations for 2,6-dimethoxybenzoic acid (2,6-DMBA) were performed using Gaussian09W [13] software to determine the stable structure at the minimum energy level. The molecular structure of 2,6-DMBA was optimized and visualized using GaussView5.0 software [14]. VEDA4.0 obtained the vibrational assignments and provided the percentage of potential energy distribution (%PED) contributions to vibrations [15]. UV-Vis absorption spectra were simulated using the time dependent (TD)-DFT method and the results were visualized in GaussView5.0. This was also employed for FMO analysis [16], which encompassed 'highest occupied molecular orbital (HOMO) and the lowest unoccupied molecular orbital (LUMO)' and global reactivity parameters and for creating and displaying the MEP reactive sites. Wavefunction analysis was conducted with Multiwfn3.8 [17], including ELF and LOL. RDG visualization was performed using the VMD tool [18]. Moreover, NBO analysis was carried out to assess electron density distribution [19]. Population analyses, including Mulliken and Natural methods, were conducted to investigate charge distribution among atoms. NLO properties were evaluated using GaussView5.0. Swiss ADME tool [20] assessed drug-likeness and PASS online tool [21] predicted the bioactivity of 2,6-DMBA. ADMET properties were also evaluated. Protein stability was performed using the Ramachandran plots through the Pro Check website [22]. Molecular docking studies of 2,6-DMBA with target proteins were conducted using AutoDock Tools 1.5.7 [23] and the results were analyzed with Discovery Studio [24] to investigate binding poses and affinities. *In silico* toxicity was predicted with the Protox 3.0 online tool [25]. To ensure convergence in calculations, the structure optimization of 2,6-DMBA initially occurred in the gas phase. This comprehensive computational and experimental strategy provides valuable insights into the molecular structure and the electronic and spectroscopic properties of 2,6-DMBA.

RESULTS AND DISCUSSION

Molecular geometry: Molecular optimization improves properties like solubility, bioavailability and selectivity [26,27]. In this study, the structure of 2,6-DMBA was optimized to find its most stable form with the lowest possible energy. The process in the gaseous phase resulted in 24 bond lengths and 39 bond angles, suggesting a balanced and stable electronic structure. Computational calculations are detailed in Fig. 1 and Table-1.

The two methoxy groups (-OCH_3), containing oxygen atoms O10 and O12, exhibit bond lengths ranging from 1.088 Å to 1.848 Å and bond angles from 105.6º to 110.8º. These values are influenced by the electronegativity of the oxygen atoms and their interactions with lone pairs. The shortest bond length, O9-H17 (0.970 Å), is associated with oxygen O9 in the carboxyl group (-COOH), where the high electronegativity of oxygen attracts electron density, thereby shortening the bond [28]. The longest bond length, O12-H17 (1.848 Å), is related to oxygen O12 in the methoxy group, where the electron density is more dispersed, resulting in a longer bond. The H17 atom,

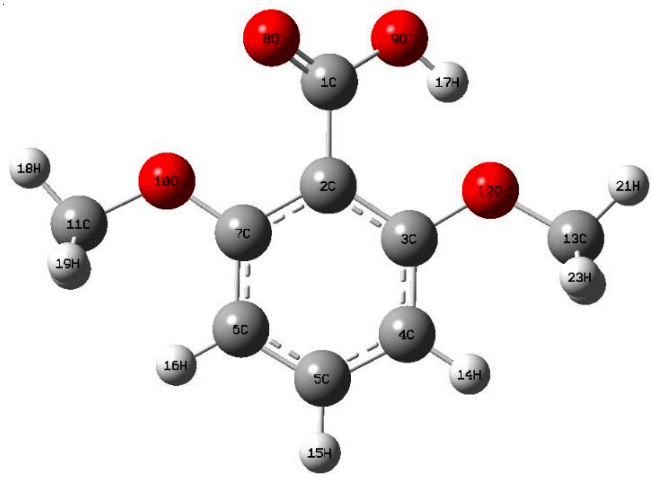

Fig. 1. Optimized structure of 2,6-dimethoxybenzoic acid (2,6-DMBA)

TABLE-1
OPTIMIZED GEOMETRICAL PARAMETERS FOR 2,6-DMBA

Atoms	Bond length (Å)	Atoms	Bond angle (º)
C1-C2	1.511	C2-C1-O8	123.5
C1-O8	1.201	C2-C1-O9	116.7
C1-O9	1.356	C1-C2-C3	122.6
C2-C3	1.410	C1-C2-C7	119.7
C2-C7	1.417	O8-C1-O9	119.8
C3-C4	1.395	C1-O9-H17	109.6
C3-O12	1.373	C3-C2-C7	117.7
C4-C5	1.390	C2-C3-C4	121.9
C4-H14	1.080	C2-C3-O12	116.0
C5-C6	1.388	C2-C7-C6	120.5
C5-H15	1.084	C2-C7-O10	116.8
C6-C7	1.401	C4-C3-O12	122.1
H6-H16	1.080	C3-C4-C5	118.8
C7-O10	1.348	C3-C4-H14	121.1
O9-H17	0.970	C3-O12-C13	119.8
O10-C11	1.422	C3-O12-H17	98.9
C11-H18	1.088	C5-C4-H14	120.0
C11-H19	1.095	C4-C5-C6	121.3
C11-H20	1.095	C4-C5-H15	119.3
O12-C13	1.427	C6-C5-H15	119.4
C13-H21	1.088	C5-C6-C7	119.8
C13-H22	1.094	C5-C6-H16	119.7
C13-H23	1.093	C7-C6-H16	120.5
O12-H17	1.848	C6-C7-O10	122.7
		C7-O10-C11	119.7
		O9-H17-O12	135.9
		O10-C11-H18	105.3
		O10-C11-H19	111.3
		O10-C11-H20	111.5
		H18-C11-H19	109.4
		H18-C11-H20	109.4
		H19-C11-H20	109.8
		O12-C13-H21	105.6
		O12-C13-H22	111.2
		O12-C13-H23	110.8
		C13-O12-H17	137.3
		H21-C13-H22	109.6
		H21-C13-H23	109.5
		H22-C13-H23	110.0

the positive site, may influence the bonding between protein and ligand, which can be analyzed in docking studies.

The benzene ring consists of sp^2-hybridized carbon atoms (C1 to C6), resulting in a planar trigonal geometry with bond angles ranging from 117.7º to 121.3º. The π-electron delocalization occurs because each sp^2 carbon in the benzene ring has an unhybridized *p*-orbital that overlaps with its neighbours. This creates a continuous π-system, allowing electrons to move freely across the ring instead of being limited to one bond. As a result, the C–C bond lengths become nearly uniform, particularly C1-C2 of 1.390 Å and C2-C3 of 1.417 Å, reflecting the stabilization provided by this electron delocalization. The -OCH_3 groups, specifically involving oxygen atoms O10 and O12, donate electron density into the aromatic ring through resonance. This interaction influences the C–O bond length (C1-O12, 1.356 Å) and nearby C–C bonds, such as C1-C2 and C2-C3, due to the redistribution of electron density. The carboxyl (-COOH) group exhibits resonance stabilization containing oxygen atoms O8 and O9. This leads to partial double-bond character in C1=O8 (1.356 Å) and C1-O9 (1.298 Å). The resonance effect reduces bond length differences and influences the bond angles (109.6º-123.4º), ensuring optimal electron distribution within the group. This delocalization results from the high electronegativity of oxygen atoms and their participation in electron sharing with the benzene ring.

The molecular structure of 2,6-DMBA exhibits a stable arrangement due to the electronegativity and resonance effects of oxygen atoms O8, O9, O10 and O12. Short bond lengths indicate strong electron attraction, while longer bonds show electron density dispersion. The minimum energy of 2,6-DMBA is -650.045 a.u., indicating a stable structure resulting from electron delocalization and favourable interactions, thereby supporting its potential in biological evaluations [29].

Vibrational assignments: The pharmaceutical industry extensively utilizes vibrational spectroscopy techniques (FT-IR & FT-Raman) to analyze drug candidates' chemical identity and conformation [30,31]. It also identifies functional groups and molecular vibrational modes [32]. Using the 3N-6 formula, 63 vibration modes were identified in 2,6-DMBA, containing 23 atoms. The scaling factor of 0.961 was incorporated into the theoretical calculations, as these calculations were conducted in the gaseous state, whereas the experimental studies were performed in the solid state [33]. The IR intensity (strength of absorption) and Raman activity (intensity of scattered light) values were calculated to understand the chemical environment of 2,6-DMBA. The purity of the bond vibrations was determined using %PED. Figs. 2 and 3 display the experimental and theoretical peaks and Table-2 lists the vibrational assignments. The experimental and theoretical peaks were comparable and the identified functional groups are discussed below:

Aromatic ring vibrations: The C-H stretching (γ) falls in the 3100-3000 cm^{-1} [34]. For 2,6-DMBA, γC-H was observed at 3094 and 3022 cm^{-1} (FT-Raman), experimentally, with %PED values of 100% and 89%, respectively. A pure stretching vibration is represented by 100%, and a less intense vibration is shown by 89%. The γC-H with 92% PED was experimentally observed at 3017 cm^{-1} (FT-IR). The corresponding theoretical γC-H frequencies were 3093, 3021 and 3019 cm^{-1}. The C=C stretching (γ) falls in the 1600-1450 cm^{-1} region [35]. For 2,6-DMBA, the

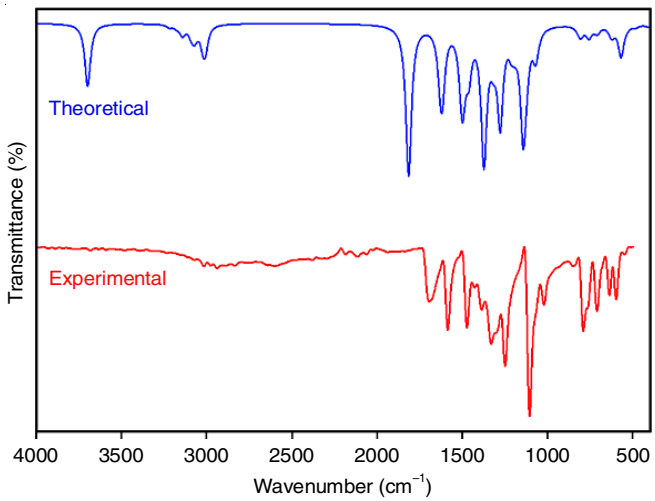

Fig. 2. FT-IR spectra of 2,6-DMBA (Exp. & Theor.)

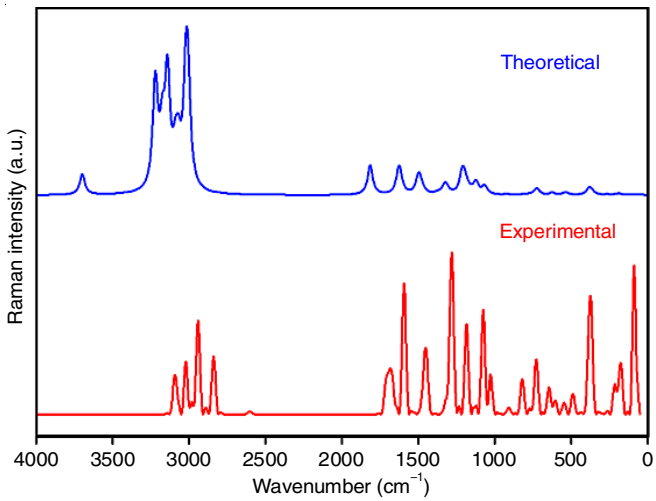

Fig. 3. FT-Raman spectra of 2,6-DMBA (Exp. & Theor.)

TABLE-2
EXPERIMENTAL AND CALCULATED VIBRATIONAL SPECTROSCOPIC DATA WITH VIBRATIONAL ASSIGNMENTS FOR 2,6-DMBA

Modes	Experimental		Theoretical		IR intensity[b]	Raman activity[c]	Vibrational assignments (%PED)*
	FT-IR	FT-Raman	Unscaled	Scaled[a]			
63	–	–	3699	3554	41	22	γ OH(100)
62	–	–	3223	3097	0	89	γ CH(94)
61	–	3094	3219	3093	1	30	γ CH(100)
60	–	–	3176	3052	1	56	γ CH(93)
59	–	3022	3144	3021	2	59	γ CH(89)
58	3017	–	3142	3019	3	64	γ CH(92)
57	–	–	3091	2970	6	32	γ CH(100)
56	2940	2942	3071	2951	7	37	γ CH(99)
55	–	–	3023	2905	11	100	γ CH(100)
54	–	2841	3009	2891	13	100	γ CH(92)
53	1697	1683	1816	1745	100	32	γ OC(86)
52	1586	1694	1630	1566	25	23	γ CC(70)
51	–	–	1618	1554	34	10	γ CC(34) + β CCC(26)
50	1474	1453	1508	1449	11	4	β HCH(47)
49	–	–	1505	1446	4	3	β HCH(48)
48	–	–	1500	1441	34	1	β HCH(57)
47	–	–	1495	1436	2	7	β HCH(76) + ω HCOC(16)
46	–	–	1492	1433	2	6	β HCH(75) + ω HCOC(17)
45	1429	–	1486	1428	1	2	β HCH(34)
44	–	–	1475	1417	0	0	β HCC(26) + β HCH(28)
43	1388	–	1463	1405	25	1	β HCC(24)
42	1332	–	1374	1320	88	1	β HOC(73)
41	–	1282	1333	1281	3	5	γ CC(74)
40	1250	–	1317	1265	12	7	γ OC(46)
39	–	–	1279	1229	61	0	γ OC(17) + β HCC(26)
38	–	1186	1217	1169	6	16	β HCC(31)
37	–	–	1210	1162	1	1	ω HCOC(50)
36	–	–	1203	1156	3	11	γ CC(10) + β HCC(32) + ω HCOC(10)
35	–	–	1191	1144	5	5	γ CC(12) + ω HCOC(32)
34	–	–	1168	1122	0	1	β HCH(29) + ω HCOC(70)
33	1107	–	1166	1120	0	1	β HCH(30) + ω HCOC(69)
32	–	–	1144	1099	69	0	γ OC(37) + β HCC(11)
31	–	1077	1124	1080	15	13	γ CC(31) + γ OC(14) + β HCC(24)
30	1022	1030	1071	1029	18	6	γ OC(29) + β CCC(21)
29	–	–	1057	1015	1	2	γ OC(73) + β CCC(10)
28	–	–	954	916	0	0	ω HCCC(72) + ω CCCC(13)

27	852	–	921	885	0	0	γ OC(67) + β CCC(11)
26	–	821	841	808	0	0	ω HCCC(72)
25	791	–	812	780	6	0	τ OCOC(29) + τ CCCC(18) + τ OCCC(31)
24	–	–	798	766	1	0	γ OC(13) + γ CC(16) + β OCO(17) + β CCC(26)
23	711	730	758	728	7	0	ω HCCC(57) + τ OCOC(24)
22	–	–	726	697	0	6	β OCO(34)
21	–	–	708	680	4	0	ω HCCC(32) + ω CCCC(56) + τ OCOC(21)
20	638	646	631	606	0	0	ω HCCC(10) + τ OCCC(55)
19	–	–	627	602	2	0	β COC(10) + ω CCCC(10)
18	599	–	624	599	4	1	β OCO(14) + β CCC(11) + β COC(16)
17	–	–	570	547	20	0	ω HOCC(75)
16	–	–	535	514	0	2	β CCC(37)
15	–	–	482	463	1	0	ω HCCC(10) + ω CCCC(16)
14	–	–	412	395	0	0	β OCC(39)
13	–	375	384	369	0	6	γ CC(19) + β COC(29)
12	–	–	366	351	0	2	γ CC(12) + β CCC(13) + β OCC(27)
11	–	–	315	302	1	0	β OCC(11) + β CCC(16) + β COC(48)
10	–	–	269	258	0	0	ω HCOC(30) + ω CCCC(23)
9	–	–	266	255	0	0	β OCC(10) + ω HCOC(10) + τ CCCC(20)
8	–	–	230	221	0	0	ω HCOC(20) + ω COCC(20) + τ CCCC(11)
7	–	–	213	204	0	0	β OCC(30) + β CCC(16) + β COC(26)
6	–	–	194	186	0	0	β OCC(26) + β CCC(33) + β COC(13)
5	–	177	187	179	0	1	ω CCCC(47)
4	–	–	101	97	0	0	ω COCC(53) + τ CCCC(11)
3	–	89	88	84	0	0	ω CCCC(10) + ω COCC(43) + τ CCCC(17)
2	–	–	60	57	1	0	ω CCCC(15) + ω OCCC(18) + ω COCC(36)
1	–	–	54	51	0	0	ω OCCC(61) + ω COCC(22)

γ = Stretching, β = In-plane bending, ω = out-of-plane bending, τ = torsion.
[a]Scaling factor 0.961 cm^{-1} for B3LYP/6-311++G (d, p) basis set. [b]Relative absorption intensities normalized with highest peak absorption equal to 100. [c]Relative Raman intensities normalized to 100. *Potential energy distribution (PED).

aromatic ring stretch was recorded at 1586 cm^{-1} (FT-IR) and 1694 cm^{-1} (FT-Raman) with 70% PED and the corresponding theoretically scaled frequency was 1566 cm^{-1}. A less intense peak was observed at 1284 cm^{-1} (FT-Raman) with 74% PED; the corresponding theoretically scaled frequency was 1281 cm^{-1}. The C-H bending (β & ω) falls at 1000-600 cm^{-1} [35]. For 2,6-DMBA, prominent peaks were observed between 640 and 950 cm^{-1}, theoretically and experimentally, with %PED values ranging from 10% to 70%.

Methoxy group vibrations: The C–O stretching (γ) typically falls in the 1300-1000 cm^{-1} region [36]. At 1250 cm^{-1}, 46% PED was observed for FT-IR and the corresponding theoretically scaled frequency was 1265 cm^{-1}. Peaks at 1077, 1030 (FT-Raman) cm^{-1} and 1022 (FT-IR) cm^{-1} were observed with up to 30% PED. The C–H stretching (methyl hydrogens) typically falls in the 3000-2800 cm^{-1} region [34]. For 2,6-DMBA, the experimentally observed FT-IR values were 2940 and 2841 cm^{-1}, with an average PED of 95%. The FT-Raman value was 2942 cm^{-1} with 99% PED. The corresponding scaled values are 2891 and 2951 cm^{-1}.

Carboxyl group vibrations: In 3600-3200 cm^{-1} region, the O–H stretching is typically observed [37]. For 2,6-DMBA, γOH was observed theoretically at 3554 cm^{-1} with 100% PED, denoting pure hydroxyl group stretching with a broad spectrum. Due to low polarizability, the O-H stretch was absent in the FT-Raman for 2,6-DMBA. The C=O stretching (carbonyl stretch) is generally observed in the 1720-1680 cm^{-1} region [38]. For 2,6-DMBA, the experimentally observed peaks were at 1697 cm^{-1} (FT-IR) and 1683 cm^{-1} (FT-Raman) with 86% PED and the corresponding scaled value was 1745 cm^{-1}. Therefore, the theoretical and experimental vibrational frequencies of the C-H aromatic ring, methoxy and carboxylic groups in 2,6-DMBA are in good agreement. Vibrational assignments for all modes were successfully determined, with the mentioned groups showing %PED values ranging from the lowest to the highest.

UV-Vis spectral studies: UV-Vis spectroscopy operates within the 200-600 nm spectrum, with UV light spanning 10 to 400 nm and visible light ranging from 400 to 600 nm [39,40]. This study calculated the UV-Vis spectrum of 2,6-DMBA using the TD-DFT method. Fig. 4 shows the theoretical UV-Vis spectrum and Table-3 presents the electronic properties of 2,6-DMBA.

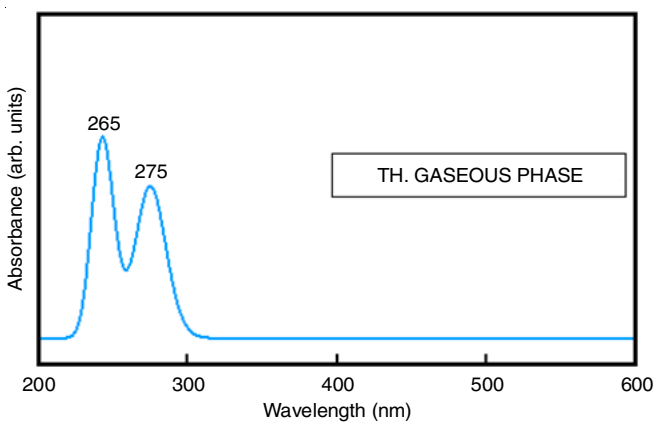

Fig. 4. UV-Vis spectrum for 2,6-DMBA

TABLE-3
UV-VIS PROPERTIES OF 2,6-DMBA USING TD-DFT/B3LYP METHOD

Solvents	Theoretical wavelength (nm)	TD/DFT			6-311++G(d,p) assignments
		Band gap (eV)	Energy (cm^{-1})	Oscillatory strength	
Gas	275	4.50	36303.82	0.0684	HOMO->LUMO (85%)
	265	4.67	37666.09	0.0126	H-2->LUMO (78%)

Two significant absorption peaks were detected at 275 nm and 265 nm, both situated in the mid-UV region of electromagnetic spectrum, attributing to the fact that a moderate amount of energy is sufficient for electron transition from HOMO to LUMO. The band gap energies corresponding to these transitions were calculated using the relation E = 1240/λ, where E is the photon energy in electron volts (eV) and λ is the wavelength in nanometers (nm). Using this formula, the absorption wavelengths of 275 nm and 265 nm correspond to band gap energies of 4.50 eV and 4.67 eV, respectively. Consequently, the compound may be classified as a moderately hard material, complemented by the molecular geometry analysis, which indicates a wide distribution of bond lengths. Moreover, these peaks are attributed to π→π* transitions, which are associated with electronic excitations between HOMO and LUMO orbitals. These transitions primarily occur within the benzene ring (C1–C6) and the carbonyl group (C1=O8), as supported by the molecular geometry findings (refer to Table-1), which highlight the bonding characteristics of these atoms. The presence of methoxy groups (O10 and O12) attached to the aromatic ring contributes to π-electron delocalization, lowering excitation energy.

Frontiers analysis: FMO analysis focuses on the energy difference between the HOMO and LUMO. The HOMO reflects the capacity to donate electrons, whereas the LUMO signifies the ability to accept electrons. The energy difference between these orbitals is key in influencing the reactivity and stability of compound; a larger gap signifies higher stability and lower reactivity. Conversely, a smaller gap suggests larger reactivity, as less energy is required for electron excitation [41-43]. Table-4 and Fig. 5 illustrate the holistic behaviour of the title compound and represent the energy of HOMO-LUMO transitions.

TABLE-4
CALCULATED ENERGY VALUE AND GLOBAL REACTIVITY PARAMETERS OF 2,6-DMBA

Parameters	TD-DFT/Gas
HOMO (eV)	-6.59
LUMO (eV)	-1.38
Ionization potential	6.59
Electron affinity	1.38
Energy gap (eV)	5.21
Electronegativity	3.98
Chemical potential	-3.98
Chemical hardness	2.60
Chemical softness	0.19
Electrophilicity index	3.04

For 2,6-DMBA, the HOMO and LUMO energies were calculated to be -6.59 eV and -1.38 eV, respectively, resulting in an energy gap of 5.21 eV. The corresponding wavelength for this energy gap of 5.21 eV was calculated using Planck's equation (eqn. 1):

$$\lambda = \frac{hc}{E} \quad (1)$$

where h represents Planck's constant (6.626×10^{-34} J.s), c denotes the speed of light (3.0×10^{8} m/s) and E is the band gap energy. The wavelength obtained using eqn. 1 is 238 nm, which complements the theoretical UV-Vis value obtained using TD-DFT and falls in the mid-UV region, predicting that the chosen compound is moderately hard and moderately reactive [44].

Ionization potential (IP) refers to energy required to remove an electron and associated with the HOMO, which acts as the electron donor. For 2,6-DMBA, the IP was calculated to be 6.59 eV. LUMO, being the electron acceptor, relates to the electron

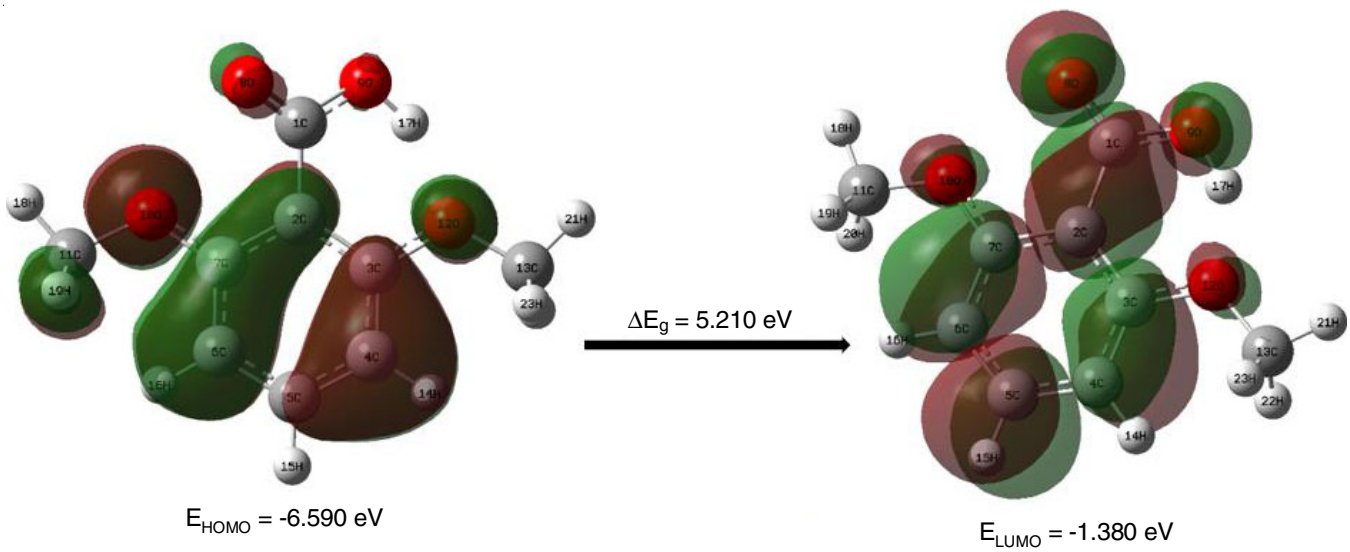

Fig. 5. FMO energy gap for 2,6-dimethoxybenzoic acid (2,6-DMBA)

affinity (EA), energy required to add an electron, which was found to be 1.38 eV [45]. Electronegativity, the tendency to attract shared electrons in a chemical bond, was 3.98 [45]. The electronegativity value of 3.98 and chemical hardness value of 2.60 suggest that the compound is moderately stable and reactive. The softness value is 0.19, which falls within the desired range of 2 [46], indicating that the material is less toxic in nature. Electrophilicity index (EI), which quantifies the tendency of a molecule to accept electrons, was calculated as 3.04 eV, indicating strong electrophilic character [47]. Since the EI value is above 1.5 eV, the chosen compound may be predicted to interact favourably with biological receptors, enzymes or metal ions [48].

Surface analyses

Molecular electrostatic potentials (MEP): MEP analysis of 2,6-DMBA in gas phase reveals the electrostatic potential regions ranging from -6.914×10^{-2} to $+6.914 \times 10^{-2}$ a.u., highlighting the electron density distribution (Fig. 6). MEP contour follows the order blue > green > yellow > red, where blue regions (positive potential) indicate electrophilic sites susceptible to nucleophilic attack, red regions (negative potential) represent nucleophilic sites prone to electrophilic attack and green regions correspond to areas of neutral potential [49,50].

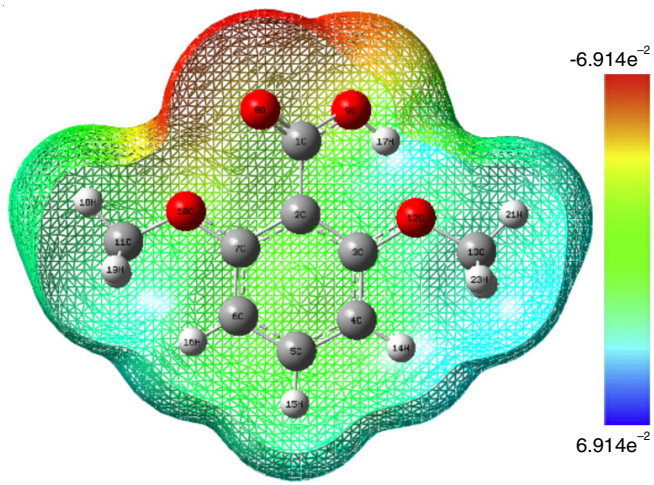

Fig. 6. Molecular electrostatic potential of 2,6-DMBA in gas phase

Oxygen atoms O8 and O9 (attached to C1, H17) and O10 (attached to C7) reside in regions of negative potential (red), making them favourable for electrophilic interactions. Hydrogen atoms H21 and H23 (attached to C13) are located in the blue areas, indicating electrophilic sites that could undergo nucleophilic attack and may participate in interactions with nucleophilic residues of biological macromolecules. Similarly, the oxygen atoms (O8, O9, O10) can act as hydrogen bond acceptors, facilitating interactions with biological macromolecules. Thus, these predictions complement the electrophilicity index in terms of potential biological interactions.

ELF and LOL: ELF and LOL maps are valuable tools for analyzing electron localization and bonding characteristics within molecules. The ELF map (Fig. 7) uses a scale from 0 to 1.0 (deep blue to red), where low values (blue) indicate minimal electron localization and high values (red) indicate strong localization [51,52]. Hydrogen atoms (H14, H15 and H21) appear in the red regions, close to 1, indicating maximum electron localization and leading to increased pauli repulsion. Carbon atoms (C2, C3, C4, C5 and C13) lie in the blue regions, indicating minimal electron localization and hence reduced pauli repulsion. The LOL map ranges from 0 to 0.8 and similarly represents regions of orbital localization from deep blue to red [53]. Hydrogen atoms (H14, H15 and H21) again appear in the red areas (high localization), while carbon atoms (C1 through C5, C13) are in blue regions, indicating lower orbital localization.

In 2,6-DMBA, ELF and LOL analyses reveal low localization regions above and below the aromatic ring, supporting the presence of delocalized π-electrons across the conjugated system [54]. Thus, ELF and LOL complement each other by illustrating electron localization and orbital behaviour, while MEP highlights the electron-rich π-regions as potential sites for electrophilic attack. These analyses provide a comprehensive understanding of the electronic behaviour and potential reactivity of molecule in biological systems.

RDG: RDG analysis of 2,6-DMBA using the VMD tool reveals the non-covalent interactions. Fig. 8 displays the RDG scatter plots and iso-surfaces of 2,6-DMBA in the gaseous phase. The plot shows that Sign(λ2)ρ is crucial for distinguishing

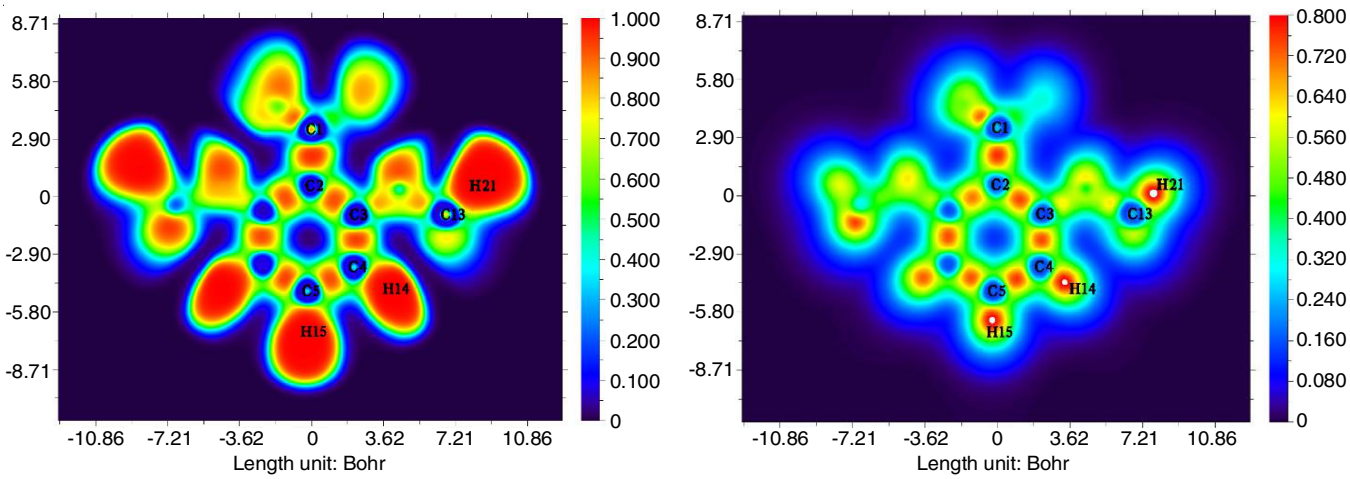

Fig. 7. ELF and LOL map of 2,6-dimethoxybenzoic acid (2,6-DMBA)

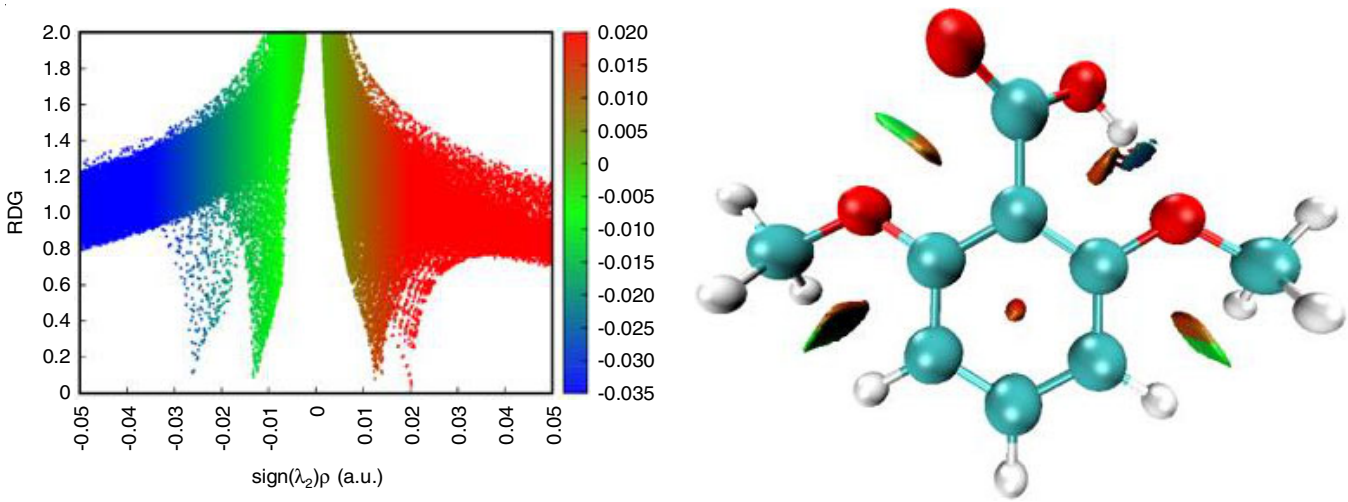

Fig. 8. RDG colour-filled map of 2,6-DMBA

between attractive and repulsive interactions. Sign(λ_2)ρ is a vital descriptor to identify non-covalent interactions, whether attractive (negative sign) or repulsive (positive sign). The colour coding is typically based on the value of Sign(λ_2)ρ, where blue indicates strong attractive interactions due to hydrogen bonding (Sign(λ_2)ρ ≤ -0.02 a.u.), green represents weak van der Waals interactions (Sign(λ_2)ρ ≈ 0) and red highlights repulsive interactions (Sign(λ_2)ρ ≥ +0.02 a.u.) [55-57].

A significant negative (λ2)ρ region peak between -0.02 and -0.035 a.u. indicates hydrogen bonding. These interactions are visualized in blue RDG iso-surfaces, marking hydrogen bonding, while green iso-surfaces depict weak van der Waals interactions contributing to molecular stability [58]. Due to a favourable non-covalent interaction, a molecule displaying extensive green and blue zones is generally considered more structurally stable. The ball-and-stick RDG isosurface model of 2,6-DMBA illustrates how hydrogen bonds (blue regions) and van der Waals interactions (green areas) are distributed around key functional groups such as –COOH and –OCH_3. These interactions improve the structural stability of the molecule and are essential for its biological activity, particularly by facilitating binding in molecular docking studies [59].

Distribution of electron density analysis: NBO analysis provides insights into the distribution of electrons within a molecule by elucidating donor-acceptor interactions, which indicate charge transfer and bonding strength, thereby contributing to the molecule's stability [60]. Selected NBO values are shown in Table-5. Transitions of electron interactions between donors and acceptors were analyzed using stabilization energy E(2), which suggests strong interactions.

TABLE-5
SELECTED E(2) OF 2,6-DMBA IN NBO BASIS BY SECOND-ORDER PERTURBATION THEORY ANALYSIS OF FOCK MATRIX

Donor	Type	ED/e	Acceptor	Type	ED/e	E(2) (kcal/mol)	E(j)-E(i) (a.u.)	F(i,j) (a.u.)
C2–C3	π	1.649	C1–O8	π*	0.194	84.70	0.02	0.062
O8	LP (2)	1.860	C1–O 9	σ*	0.086	30.12	0.62	0.124
C4–C5	π	1.669	C2–C3	π*	0.429	24.34	0.26	0.073
C2–C3	π	1.649	C1–O8	π*	0.194	17.51	0.29	0.066
C2–C3	π	1.649	C4–C5	π*	0.347	15.34	0.28	0.058
O9	LP (2)	1.895	C1–O8	π*	0.194	14.06	0.42	0.070
O12	LP (2)	1.888	C2–C3	π*	0.429	13.62	0.38	0.070
O9	LP (1)	1.961	C1–C2	σ*	0.074	7.13	0.95	0.074
O10	LP (1)	1.952	C6–C7	σ*	0.030	6.36	1.03	0.072
O12	LP (1)	1.952	C3–C4	σ*	0.032	6.35	1.04	0.073
C6–H16	σ	1.978	C2–C7	σ*	0.033	3.96	1.05	0.058
C1–O8	π	1.977	C2–C3	π*	0.429	3.82	0.38	0.038
C4–C5	σ	1.979	C3–O12	σ*	0.028	3.68	1.06	0.056
C3–C4	σ	1.980	C2–C3	σ*	0.033	3.40	1.23	0.058
C11–H18	σ	1.991	C7–O10	σ*	0.026	3.19	0.88	0.047
C13–H21	σ	1.991	C3–O12	σ*	0.028	3.10	0.89	0.047
C1–C2	σ	1.975	C6–C7	σ*	0.030	2.91	1.17	0.052
C2–C7	σ	1.970	C6–C7	σ*	0.030	2.86	1.23	0.053
O12	LP (1)	1.888	C13–H23	σ*	0.023	2.57	0.86	0.042
O10	LP (1)	1.952	C11–H19	σ*	0.017	2.48	0.87	0.042
C5–C6	σ	1.979	C4–H14	σ*	0.013	2.41	1.11	0.046

The most significant delocalization occurs between the bonding orbital of C2-C3 and the antibonding orbital of C1-O8 (π-π*), with high stabilization energy of 84.7 kcal/mol, indicating the strong π-π* conjugation. Another significant interaction involves lone pair electrons on O8 donating to the antibonding orbital of C1-O9 (LP→σ*), contributing 30.12 kcal/mol. Due to their lone pair electrons and high donor strength, these interactions identify oxygen atoms, especially O8 and O9, as key nucleophilic regions in the MEP study (refer to Fig. 6). At the same time, the antibonding orbitals of C1–O8 and C1–O9 act as electrophilic sites by accepting electron density, thus serving as charge-accepting centers. These donor-acceptor interactions are supported by RDG analysis, which shows green-to-blue isosurfaces around the oxygen atoms, signifying attractive interactions such as hydrogen bonding (Fig. 8). Other notable transitions include π→π* interactions from C4-C5 to C2-C3 of 24.34 kcal/mol and from C2-C3 to C4-C5 of 15.34 kcal/mol, all contributing to the molecular stability. These findings reveal nucleophilic (O8, O9, O12) and electrophilic (C1-O8, C1-O9) regions within 2,6-DMBA, suggesting strong binding potential through hydrogen bond and π-π stack. These interactions are essential when binding to biological targets such as enzymes, receptors or proteins involved in Alzheimer's disease, which supports its neuroprotective potential [61]. These transitions entail the movement of charge from electron donor orbitals to electron acceptor orbitals, highlighted by their higher stabilization energy values and the overall stability of 2,6-DMBA [62].

Population analyses: MPA and NPA were conducted for 2,6-DMBA with results detailed in Table-6. These analyses reveal the electronic charge distribution within the compound, pinpointing either electron-rich (negatively charged) or electron deficient (positively charged) areas, thereby providing insight into the reactivity and interaction potential of molecule [63,64]. According to the Mulliken analysis, atomic charges varied from -0. 4685 to + 0.3339 (in electrons, e), where the lowest charge was found on C5 (-0.4685) and the highest on C6 (+ 0.3339). The NPA showed a charge range from -0. 6809 to +0.4667 (e), with O9 (-0.6809) having the highest electron density and H17 (+0.4667) displaying the most significant electron deficiency. All hydrogen atoms presented positive charges in both analyses, while oxygen atoms exhibited the most negative values. Carbon atoms in the aromatic ring, specifically C2, C4 and C6, exhibited positive and negative charges. A comparison of MPA and NPA is illustrated in Fig. 9.

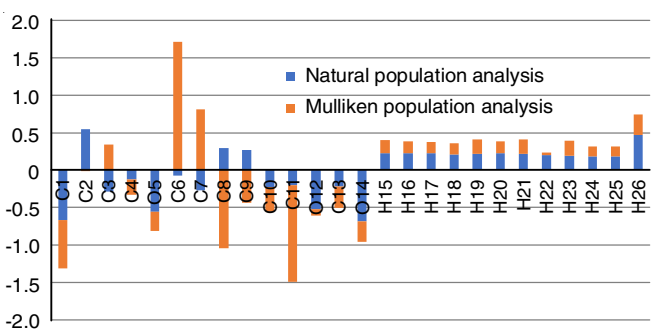

Fig. 9. Population charge distribution plot for 2,6-DMBA

TABLE-6
MULLIKEN AND NATURAL ATOMIC POPULATION IN THE GAS PHASE FOR 2,6-DMBA

Atoms	Mulliken population (e)	Natural population (e)
C1	-0.135472	0.77876
C2	0.210608	-0.24260
C3	-0.404038	0.34698
C4	0.309044	-0.27454
C5	-0.46850	-0.15912
C6	0.333976	-0.26958
C7	-0.37344	0.37345
O8	-0.251015	-0.54431
O9	-0.159536	-0.68097
O10	-0.093215	-0.53701
C11	-0.285996	-0.20254
O12	-0.227039	-0.55582
C13	-0.263311	-0.19450
H14	0.155996	0.21333
H15	0.175705	0.21325
H16	0.164544	0.21733
H17	0.291376	0.46678
H18	0.195539	0.19292
H19	0.159187	0.16464
H20	0.150627	0.17685
H21	0.18487	0.19687
H22	0.165696	0.14010
H23	0.164394	0.17972

The notably negative charges on O8 and O9 align with the NBO results, indicating strong interactions between lone pairs (LP) and antibonding (σ*) orbitals of C1 and the O9 bond, as well as between π(C2-C3) and π*(C1-O8). This interaction contributes to the stabilization energy (Table-5). The substantial negative charge on these atoms signifies their role as electron rich donors involved in charge delocalization, corroborating the charge distribution observed in the MPA and NPA [65]. C2 and C3 exhibit donor characteristics, with C2 showing a positive Mulliken charge (+0.2106) and a negative NPA (-2426), while C3 displays a negative Mulliken charge (-0.4040) and a positive NPA (+0.3469), indicating their roles in π-electron donation. Conversely, O8 in the C1-O8 bond shows significant negative charges (-0.2510 MPA, -0.5443 NPA), reinforcing its nature as an electron acceptor, consistent with the donor-acceptor interaction. This charge distribution supports the NBO findings, where electron-rich donor regions, such as π(C2-C3), interact with electron-deficient acceptor regions like the π*(C1-O8) orbital, contributing significantly to the stabilization of 2,6-DMBA. Surface analyses using MEP, ELF and LOL also support these findings by visually revealing negative potential near O8 and O9 and positive regions near hydrogens (MEP), localized lone pairs on O8 and O9 (ELF) and delocalization along the C2-C3 and C1-O8 bonds (LOL), consistent with the charge distribution and donor-acceptor interactions.

Non-linear optical analysis: The key NLO parameters include dipole moment, signifying the charge separation within the molecule; polarizability, measuring the degree of electron cloud distortion; and first-order hyperpolarizability, representing the non-linear optical response of molecule [66]. These values provide insight into the electronic behaviour of mole-

cules. Dipole moment of 2.595 D, polarizability (α) of 4.231 × 10^{-23} esu and first-order hyperpolarizability (β) of 3.039 × 10^{-30} esu, respectively (Table-7). The hyperpolarizability value of 2,6-DMBA was compared with that of urea, a standard NLO compound, with a β value of 0.927 × 10^{-30} esu [67]. The results revealed that the hyperpolarizability of 2,6-DMBA is four times higher than urea (β is 4× higher) indicating that it is a moderately reactive compound suitable for biological activity, as confirmed by the UV analysis. This enhanced hyperpolarizability suggests a significant non-linear optical activity, indicating charge transfer within the molecule. The elevated hyperpolarizability in 2,6-DMBA is attributed to π-electron delocalization across electron-donating and electron-withdrawing groups, as supported by NBO analysis. This analysis confirms strong intramolecular charge transfer (ICT), particularly from the lone pairs of oxygen atoms (O8, O9, O10 and O12) to the π* orbitals of the aromatic system. Such ICT enhances the molecule's polarization, which correlates with increased pharmacological efficacy, especially in neurological applications, receptor binding and membrane interaction [68].

TABLE-7
CALCULATED DIPOLE MOMENT μ(D), POLARIZABILITY (α) AND FIRST ORDER HYPER POLARIZABILITY (β)

Parameters	Gas
Dipole moment μ(D)	2.595
Polarizability (α)	4.231 × 10^{-23}
First-order hyperpolarizability (β)	3.039 × 10^{-30}
Comparison with urea (0.927 × 10^{-30})	4 > Urea

In addition to its potential treatment for AD, it can also be utilized for advanced imaging techniques, such as multiphoton microscopy, which enables the non-invasive visualization of amyloid-beta (Aβ) plaques, a hallmark of AD pathology due to its NLO active nature [1]. Molecules with significant NLO activity can function as fluorescent probes to monitor drug distribution across the BBB, a major hurdle in central nervous system drug development, as further discussed in the ADMET properties section. Moreover, the moderate HOMO–LUMO gap (5.21 eV) suggests a balance between chemical stability and reactivity, supporting both low toxicity and sufficient electronic flexibility for the biological interactions [44,46]. Therefore, the NLO behaviour of 2,6-DMBA, along with charge transfer capability and electronic stability, provides a multifaceted assessment of its potential bioactivity and therapeutic value in neurodegenerative disease [69].

ADMET properties: Compound 2,6-DMBA meets several key pharmacokinetic criteria for this application. For CNS efficacy, a drug must have properties such as oral bioavailability, brain permeability and favourable metabolic characteristics. ADMET properties, along with standard values and activity, are shown in Table-8. SwissADME predicts that 2,6-DMBA exhibits high gastrointestinal (GI) absorption, indicating good oral absorption. It is also expected to cross the blood-brain barrier (BBB), a protective layer that separates the bloodstream from the brain, which controls the passage of molecules through it. The ability to penetrate the BBB is vital for CNS medications

TABLE-8
ADMET PARAMETERS OF 2,6-DMBA

Descriptor	Desired value/activity	Value
Hydrogen bond donor (HBD)	<10	1
Hydrogen bond acceptor (HBA)	<5	4
M log P	<4.15	1.06
W log P	≤5	1.40
Molar refractivity	40-130	46.39
Number of rotatable bonds	<10	3
Lipinski violation	0	0
Ghose	0	0
Veber	0	0
Egan	0	0
Molecular weight	<500	182.17 g/mol
Bioavailability score	0.11-0.85	0.85
TPSA	≤140 Å^2	55.76 Å^2
Blood-brain barrier permeant	Active/Inactive	Active
GI absorption	High/low	High
P-glycoprotein	Yes/No	No
CYP1A2	Yes/No	No
CYP2C19	Yes/No	No
CYP2C9	Yes/No	No
CYP2D6	Yes/No	No
CYP3A4	Yes/No	No
PAINS	0	0
Brenk	0	0
Synthetic accessibility	<5	1.37

[70,71]. Fig. 10 depicts the boiled egg plot for 2,6-DMBA. Boiled egg model supports this, positioning 2,6-DMBA in the "yolk" zone, which indicates promising brain penetration capability. This assessment relies on two key properties: WLogP or Wildman and Crippen Log P, which is a logarithm of the partition coefficient between octanol and water and predicts how well a molecule balances water and fat solubility. Topological polar surface area (TPSA) measures a molecule's polar (hydrophilic) surface and helps predict its ability to be absorbed, cross membranes or reach the brain. Compounds with moderate lipophilicity and low polarity generally cross biological membranes, including the BBB, more effectively. With a WLogP of 1.40 and a TPSA of 55.76 Å^2, 2,6-DMBA falls within the preferred range, signifying a favourable balance between solubility and membrane penetration [72,73].

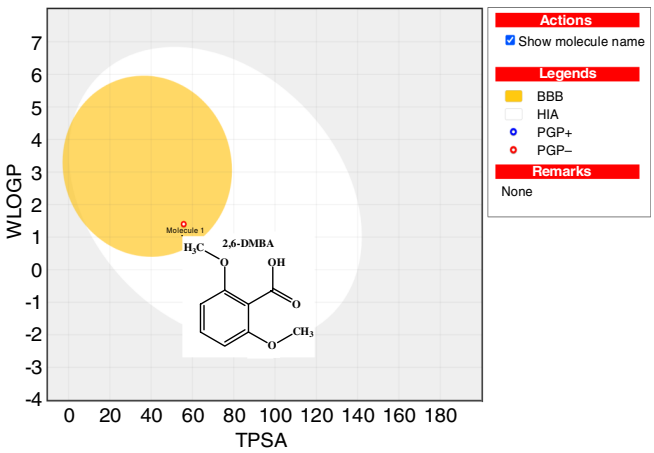

Fig. 10. Boiled egg plot for 2,6-DMBA

Furthermore, 2,6-DMBA is not a substrate for P-glycoprotein (P-gp), a transport protein that can pump drugs from the brain and intestines, often limiting their effectiveness. Its lack of interaction with P-gp enhances its retention in the brain and boosts its overall efficacy as a neuroactive agent. This characteristic also minimizes drug resistance and the risk of adverse drug-drug interactions (DDI). DDIs occur when one medication influences the metabolism or action of another, potentially impacting the efficacy or toxicity. A primary contributor to DDIs is the inhibition or induction of cytochrome P450 (CYP) enzymes, which metabolize numerous drugs in the liver. Notably, 2,6-DMBA does not inhibit significant CYP enzymes, including CYP1A2, CYP2C19, CYP2C9, CYP2D6 and CYP3A4, which are vital for drug metabolism. When these enzymes are inhibited, it can result in DDIs, with one drug affecting another's breakdown and leading to unexpected side effects or diminished efficacy. The minimal interaction of 2,6-DMBA with CYP enzymes indicates a low risk of metabolic issues, which is particularly important for elderly patients using multiple medications [74].

2,6-DMBA complies with Lipinski's Rule of Five (LRO5) without any infractions regarding drug-likeness features. It contains one hydrogen bond donor (HBD), four hydrogen bond acceptors (HBA), and three rotatable bonds within the specified ranges. Molecular weight (182.17 g/mol) and molar refractivity (46.39) align with the expected range. The compound also meets other crucial drug-likeness filters, including the Ghose, Veber and Egan rules, which evaluate molecular weight, polarity, flexibility and lipophilicity to assess oral bioavailability. A bioavailability score of 0.85 indicates that the title compound may be an effective oral compound for biological systems. Furthermore, no PAINS (pan-assay interference compounds) or Brenk structural alerts were identified for 2,6-DMBA, suggesting that it is unlikely to produce false positives in biological assays. Synthetic accessibility score of 1.37 indicates that 2,6-DMBA, which is relatively uncomplicated to synthesize in the laboratory, is beneficial for future drug development [75-77]. As previously discussed in FMO studies (Table-4), predicted values indicate that the compound is non-toxic at the electronic level. Calculated parameters based on several key pharmacokinetic criteria, such as physico-chemical characteristics, oral bioavailability, metabolic stability and electronic properties, indicate that 2,6-DMBA may be a promising and non-toxic drug candidate for developing treatments for Alzheimer's dementia.

Cytotoxicity *in vitro*: MTT (3-(4,5-dimethylthiazol-2-yl)-2,5-diphenyltetrazolium bromide) assay on 2,6-DMBA was conducted to evaluate the potential cytotoxic effect against L929 mouse fibroblast cells [78]. Cell viability was assessed at concentrations ranging from 25 to 500 µg/mL, as summarized in Table-9. The compound maintained over 99% cell viability, indicating it does not adversely affect cellular metabolic activity and exerts minimal toxicity within this concentration range. The IC_{50} value, the concentration at which cell viability is reduced by 50%, was estimated to be 2300 ± 1.526 µg/mL, using GraphPad Prism software, suggesting that very high doses are required to induce cytotoxic effects [79]. Fig. 11 shows the relationship between 2,6-DMBA concentration and cell viability and Fig. 12 presents a morphological image of cells exposed to 2,6-DMBA.

TABLE-9
In vitro CYTOTOXICITY OF 2,6-DMBA

Tested concentration (µg/mL)	Absorbance 570 nm	Cell viability (%)	Standard error
500	0.548	99.4	0.49
250	0.553	99.94	0.22
100	0.551	100	0.48
50	0.552	100	0.28
25	0.556	100.24	0.16
Negative control	0.555	100.06	0.78
Positive control	0.245	43.54	1.08

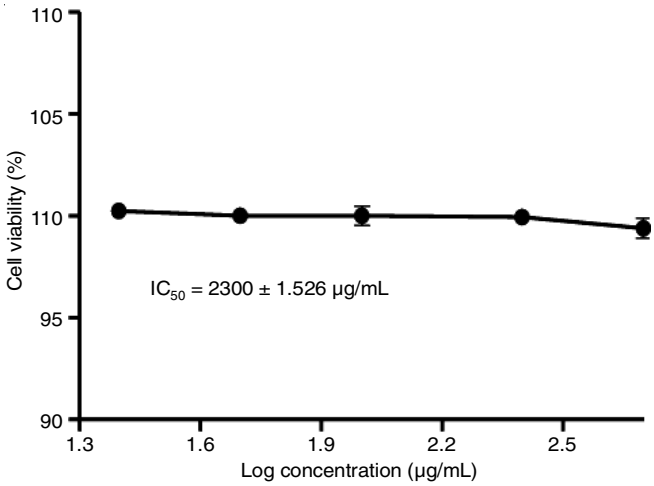

Fig. 11. Graphical representation of 2,6-DMBA with IC_{50} value

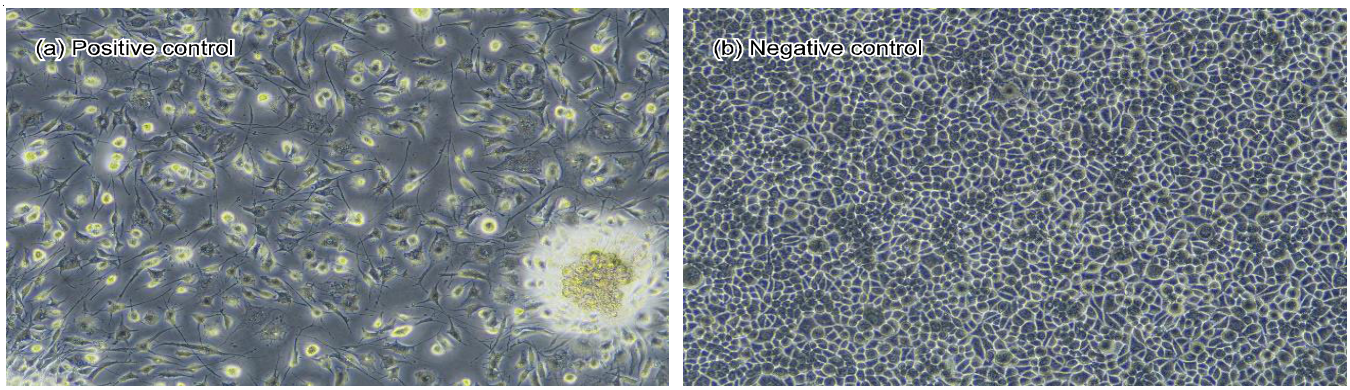

Fig. 12. Morphological representation of 2,6-DMBA with L929 cell line

In silico toxicity analysis using ProTox 3.0 [25] predicted that 2,6-DMBA falls under toxicity Class 4, corresponding to a predicted LD_{50} (Lethal dose for 50% of animals) of 2000-5000 mg/kg. Class 4 is less toxic when compared to more hazardous cases, ranging from 1 to 3. Although IC_{50} and LD_{50} reflect toxicity in different biological systems, cell culture *versus* whole organism, their consistently high values suggest a favourable safety profile. LD_{50} prediction complements the IC_{50} findings, reinforcing the idea that 2,6-DMBA is non-toxic both *in vitro* and *in vivo*. Furthermore as evidenced by a chemical softness value of 0.19, which theoretically supports its lower toxicity. The findings suggest that 2,6-DMBA is a safe and non-toxic, highlighting its potential for biomedical and drug development applications.

Ramachandran plot: The structural evaluation of the chosen protein targets through Ramachandran plot analysis provided essential insights into their suitability for molecular docking simulations [80]. Ramachandran plot is depicted in Figs. 13 and 14. AD proteins, namely 6EQM (BACE-1) and 2C5G (acetylcholinesterase), were selected from the Protein Data Bank [81], exhibit excellent stereochemical quality, with over 90% of their residues located in favoured regions and none in disallowed zones, thereby affirming their structural integrity. This high degree of refinement is apparent in the 6EQM and 2C5G structures, with respective resolutions of 1.35 Å and 1.95 Å, which underpins the reliability of the docking outcomes. These proteins were selected for their direct involvement in the pathophysiology of neurodegenerative disorders, particularly AD [82]. The validated protein structures provide a solid foundation for docking-based interaction investigations, highlighting the importance of 2,6-DMBA as a promising candidate in advancing multitarget therapeutics for neurological conditions.

Molecular docking studies: In drug discovery, identifying effective therapeutic candidates remains a significant challenge. Molecular docking plays a crucial role by simulating ligand-protein interactions and predicting binding energies, thereby streamlining the identification of promising compounds towards therapeutic strategies [83,84]. Fig. 15a-d visually represent the ligand-protein interactions in 2D and 3D and the docking result values are presented in Table-10.

Using the PASS online tool [21], 2,6-DMBA shows the activity towards AD indicating its potential neuroactive properties. Additionally, 2,6-DMBA has been associated with other neurological effects, such as tremor suppression, pain modulation and cognitive enhancement. To explore the therapeutic relevance in Alzheimer's, 2,6-DMBA was docked against two protein targets, 6EQM (β-secretase 1 or BACE-1) and 2C5G (acetylcholinesterase or AChE) [85,86]. The docking results revealed that 2,6-DMBA exhibits binding energy of -7.20 kcal/mol (BACE-1) and -7.05 kcal/mol (AChE). The same proteins were docked for the commercially available drug rivastigimine [87], with the binding energy of -5.40 kcal/mol for BACE-1 and -6.12 kcal/mol for AChE. Since the binding energies of the title compound are greater than that of the commercially available drug, it may predict the suitability of the title compound towards AD.

For 6EQM protein, 2,6-DMBA formed two conventional hydrogen bonds with TYR71 (tyrosine) and ASP32 (aspartic acid), key residues in amyloid-β aggregation. This suggests that 2,6-DMBA may disrupt plaque-associated interactions, that is, molecular contacts that drive amyloid plaque formation, potentially reducing harmful protein clumping in the brain. For 2C5G protein, 2,6-DMBA interacted with ASP369 (aspartic acid) and SER122 (serine), key residues in cholinergic signaling, a pathway that relies on the neurotransmitter acetylcholine to regulate memory and cognition. This suggests that 2,6-DMBA may help modulate these neural pathways, potentially supporting cognitive function. Docking analysis revealed that 2,6-DMBA binds effectively at the active sites of both proteins, forming stable hydrogen bonds, particularly between the hydroxyl hydrogen (H17) and carboxylate oxygen atoms (O8) of ASP32 and ASP369 as well as with the hydroxyl oxygen

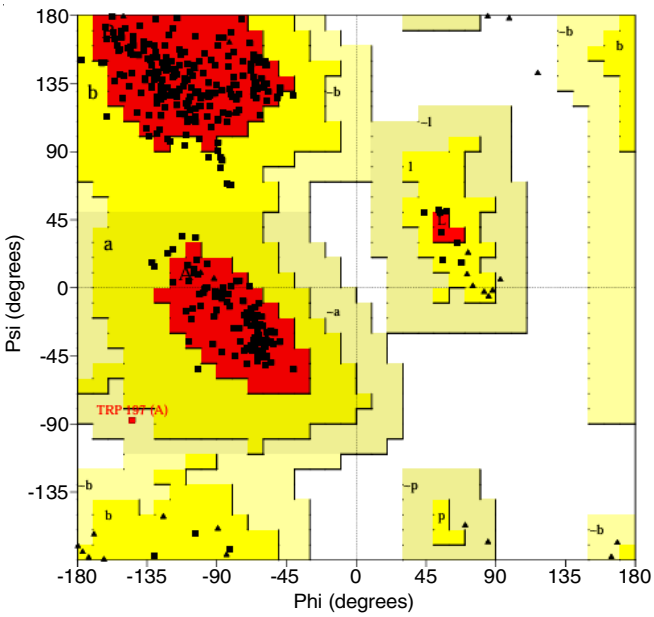

Fig. 13. Ramachandran plot for protein 6EQM

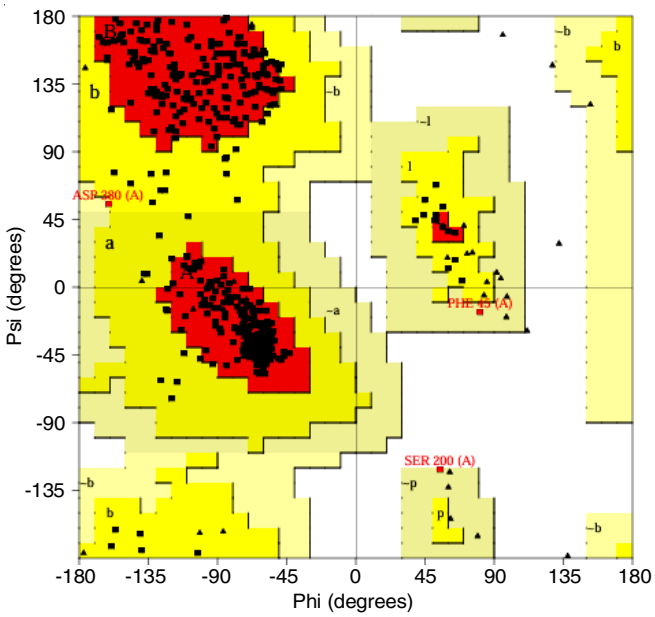

Fig. 14. Ramachandran plot for protein 2C5G

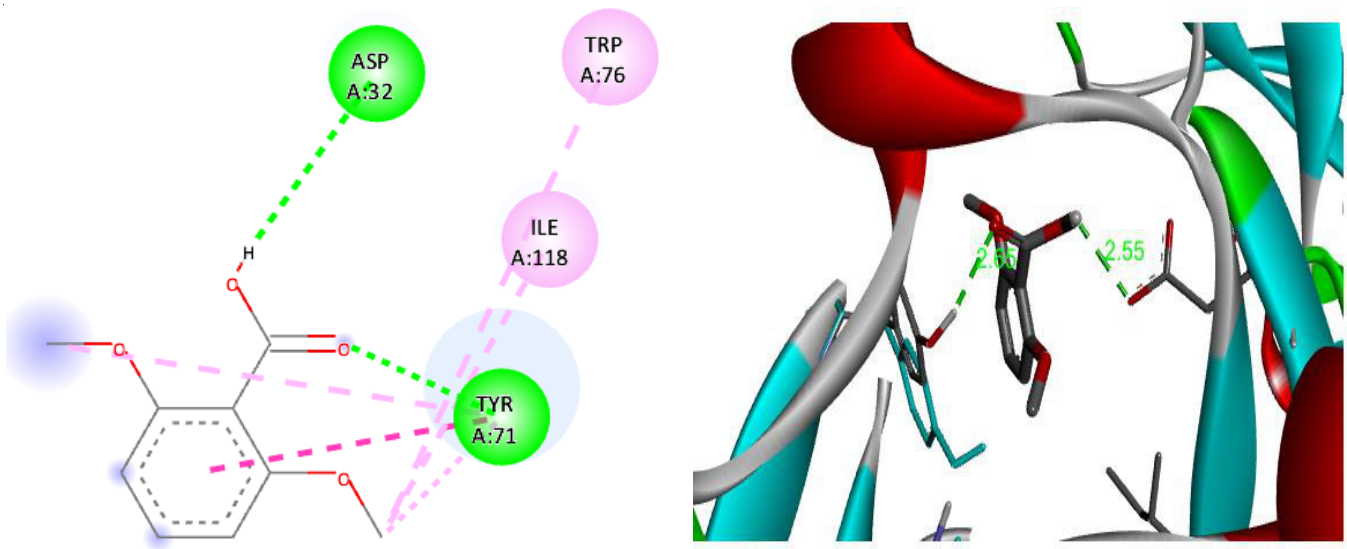

Fig. 15a. Docking conformation (2D & 3D) of 2,6-DMBA with 6EQM protein

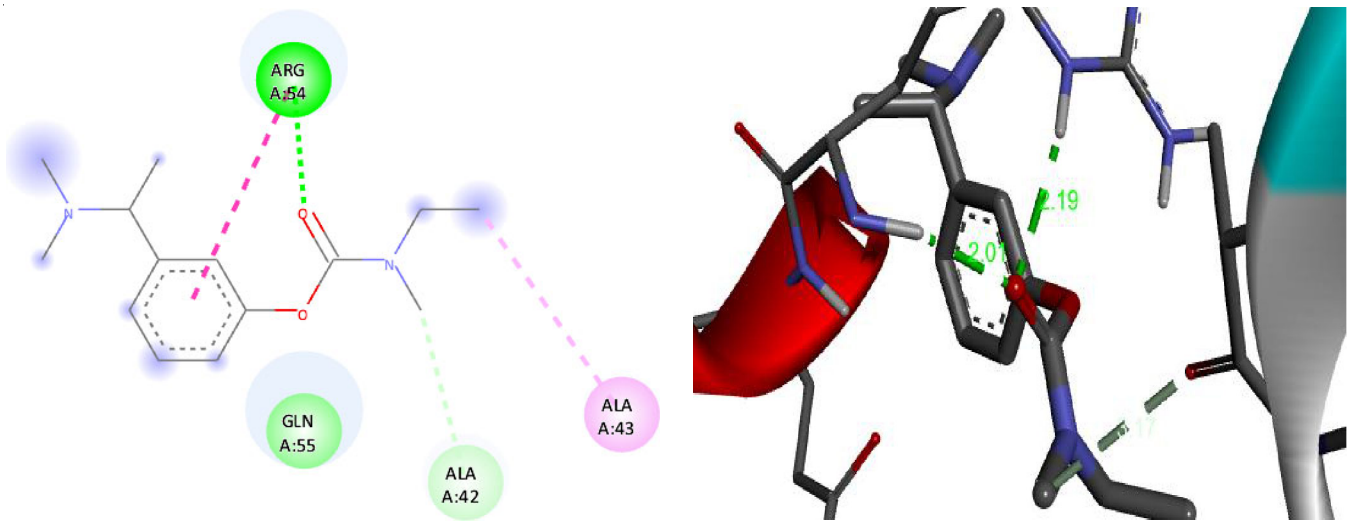

Fig. 15b. Docking conformation (2D & 3D) of standard drug with 6EQM protein

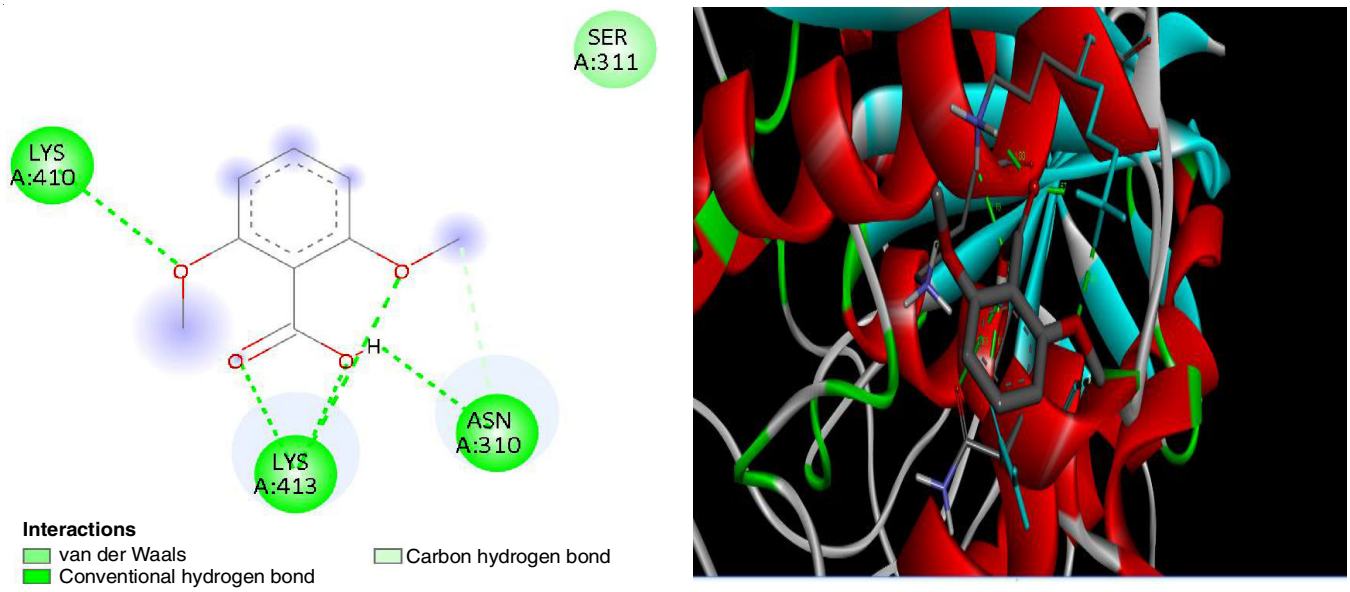

Fig. 15c. Docking conformation (2D & 3D) of 2,6-DMBA with 2C5G protein

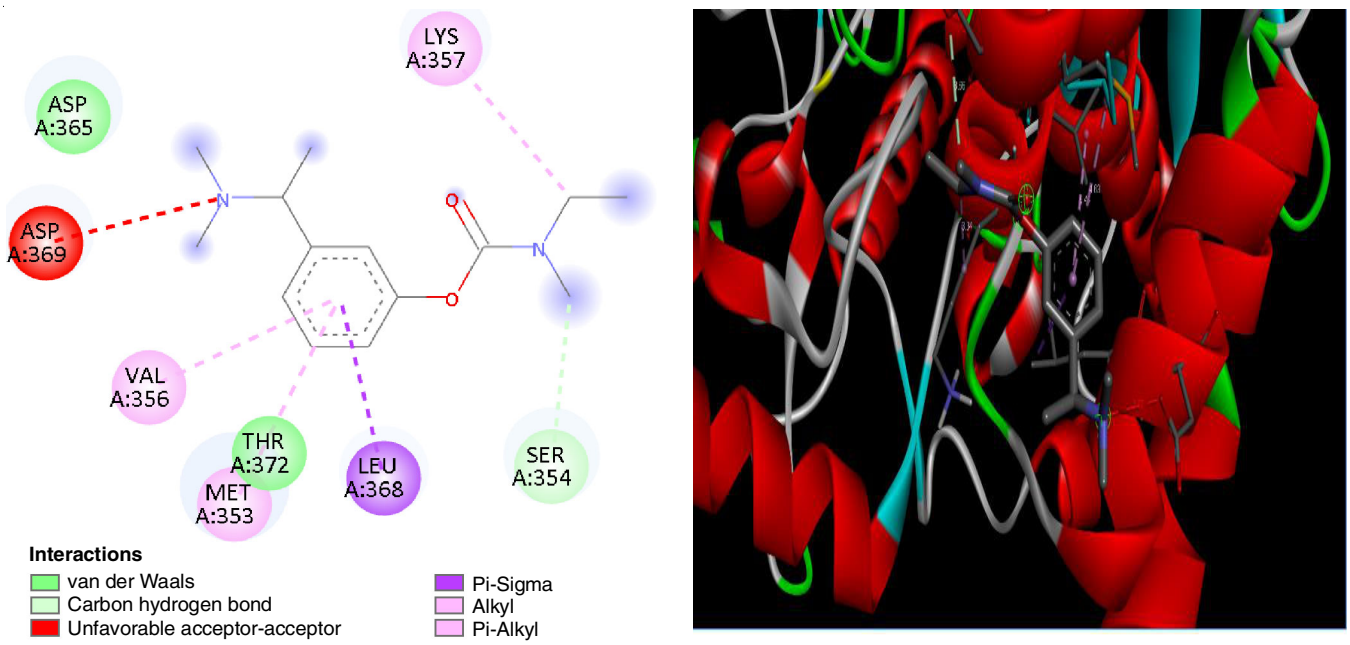

Fig. 15d. Docking conformation (2D & 3D) of standard drug with 2C5G protein

TABLE-10
MOLECULAR DOCKING OF 2,6-DMBA COMPARED WITH THE STANDARD DRUG

Protein	Property	Ligand	Bonded residues	Bonded distance (Å)	Binding energy (kcal/mol)	Reference RMSD (Å)
6EQM	Dementia treatment	2,6-DMBA (title compound)	ASP32	2.55	-7.20	32.48
			TYR71	2.65		
		Rivastigmine (standard drug)	ARG54	2.01	-5.40	5.47
2C5G	Dementia treatment	2,6-DMBA (title compound)	ASP369	2.77	-7.05	93.41
			SER122	1.96	-6.84	93.29
		Rivastigmine (standard drug)	LYS413	1.87	-6.12	67.00
			LYS413	1.86	-5.94	67.14
			LYS410	1.80	-5.80	67.55

(O9) of SER122. These interactions support its role as a dual-action inhibitor, targeting both amyloid and cholinergic pathways in AD [88].

The binding behaviour of 2,6-DMBA is supported by its optimized molecular structure, with the shortest bond length (0.972 Å) observed between O9 and H17, confirming H17 as a hydrogen bond donor (HBD). The electronegative oxygen atoms O8, O9, O10 and O12 functioned as hydrogen bond acceptors (HBA). As determined by drug likeness analysis, 2,6-DMBA possesses one HBD and four HBA. These features facilitated stable hydrogen bonding with protein residues. The conventional hydrogen bond observed in the docking interactions occurred specifically between H17 of ligand (2,6-DMBA), reinforcing the stabilizing nature of these interactions. FMO analysis further complemented these findings. LUMO was found to be localized over the carboxylic acid group, particularly around O8 and O9, suggesting this site as the primary region for electrophilic interaction during the protein binding. Moreover, the moderate HOMO-LUMO energy gap indicates a favourable balance between molecular reactivity and stability, both are the crucial characteristics for biologically active compounds. The MEP surface supported these observations by showing a positive potential region near H17, aligning with its electrophilic hydrogen bond donor role. RDG analysis highlights that electron-rich sites (O8, O9, O10) and electron-deficient sites (H21, H23) also correspond to key hydrogen bonding interactions with ASP and SER residues observed from docking. MPA and NPA revealed a partial positive charge on H17 and a negative charge on O10, confirming its involvement in conventional hydrogen bonding. These studies and docking results suggest that 2,6-DMBA shows promising ligand-protein interactions, indicating its potential suitability for anti-dementia treatment.

Conclusion

The structural, vibrational, electronic and topological studies, as well as biological evaluations of 2,6-dimethoxybenzoic acid (2,6-DMBA) were performed using DFT techniques with the Gaussian 09W package and the B3LYP/6-311++G(d,p) basis set. The optimized structure of 2,6-dimethoxybenzoic acid has been determined. Geometrical parameters of 2,6-DMBA offer insights into its structural analyses and biological activity. FT-IR and FT-Raman spectral analyses were conducted, applying a scaling factor of 0.961 to the theoretical values because the experimental and theoretical analyses were performed in different phases. Pure C-H stretching peak was observed at 3094

cm^{-1} and 3093 cm^{-1} in both experimental and theoretical FT-Raman spectra, indicating pure stretching due to 100% PED values. Furthermore, the theoretical and experimental findings identified O-H and C=O stretching vibrations for FT-IR and FT-Raman analyses, respectively, showing the consistency between experimental and theoretical spectroscopic data. From UV-Vis analysis, the absorption peak at 238 nm, which is in the mid-UV region, indicates moderate stability and reactivity of the title compound. FMO studies provide essential insights into charge transfer and the biological activity of molecule. The calculated energy gap from HOMO-LUMO analysis is 5.21 eV. The UV and FMO studies suggest that the compound exhibits moderate reactivity, making it suitable for targeting specific biological activities. The calculated chemical hardness of 2.6 eV indicates moderate stability, while the low chemical softness value of 0.19, under 2, signifies its non-toxic nature. This is reinforced by the electrophilicity index (3.04) above 1.5, indicating that the title compound exhibits a moderate electrophilic nature suitable for biological activity. MEP map highlighted the electrophilic attack sites on the oxygen atoms (O8 and O9) and the nucleophilic attack sites on the hydrogen atoms (H21 and H23). RDG analysis complements this by revealing electron-rich regions (O8, O9, O10) and electron deficient sites (H21, H23), indicating potential areas for electrophilic, nucleophilic and hydrogen bonding interactions. Hydrogen atoms (H14, H15, H21) were seen in the red region of the ELF map, indicating the maximum Pauli's repulsion and carbon atoms (C2, C3, C4, C5, C13) were in the blue region, indicating minimum Pauli's repulsion. The H14, H15 and H21 atoms were seen in the red region of the LOL map, indicating maximum electron localization and C1 through C5, C13 atoms were in the blue region, suggesting low electron localization, which complements ELF studies. A notable peak in the negative $(\lambda 2)\rho$ region, between -0.02 and -0.035 a.u., indicates the presence of hydrogen bonding. Combined topological studies MEP, ELF, LOL and RDG predict possible chemical bonding and interactions, crucial for the biological activity of 2,6-DMBA. NBO analysis evaluated electron interactions between donors and acceptors, revealing the highest stabilization energy of 84.7 kcal/mol during electron transitions between π(C2-C3) and π^*(C1-O8). Strong interactions between the electron donor and acceptor were indicated by the high stabilization energy values in NBO analysis. MPA and NPA results indicate significant charge centres in 2,6-DMBA, including C5 (-0.4685 e), C6 (+0.3339 e), O9 (-0.6809 e) and H17 (+0.4667e), which corroborate the NBO findings. These values confirm donor-acceptor interactions and overall electronic stability of the chosen compound. The higher hyperpolarizability (3.039×10^{-30} esu) of 2,6-DMBA compared to urea suggests enhanced electronic responsiveness, which may support its potential for biological activity. ADMET studies that evaluate several key pharmacokinetic criteria including LRO5, boiled egg, BBB, GI absorption and bioavailability scoring show that the calculated parameters for 2,6-DMBA fall within the desirable range, indicating favourable properties for drug development in AD treatment. Both *in vitro* (IC_{50} = 2300 µg/mL) and *in silico* (LD_{50} = 2000-5000 mg/kg) data support a favourable safety profile, suggesting that 2,6-DMBA is a non-toxic compound with significant potential for biomedical applications. The stability of Alzheimer's dementia proteins, such as 6EQM and 2C5G, was assessed using the Ramachandran plot, confirming suitability for docking with the selected ligands. Molecular docking studies of 2,6-DMBA with the target proteins 6EQM and 2C5G showed binding energies of -7.20 kcal/mol and -7.05 kcal/mol, respectively. The binding energy of 2,6-DMBA was found to be greater than that of standard drug (rivastigmine), which showed -5.40 kcal/mol *(*6EQM*)* and -6.12 kcal/mol *(*2C5G*)*, respectively. These studies and docking results suggest that 2,6-DMBA shows the promising ligand-protein interactions, indicating its potential suitability for anti-dementia treatment.

CONFLICT OF INTEREST

The authors declare that there is no conflict of interests regarding the publication of this article.

REFERENCES

1. Alzheimer's Association, *Alzheimers Dement.*, **19**, 1 (2023); https://doi.org/10.1002/alz.12925
2. Q. Wu, D.-X. Fu, A.-J. Hou, G.-Q. Lei, Z.-J. Liu, J.-K. Chen and T.-S. Zhou, *Chem. Pharm. Bull.*, **53**, 1065 (2005); https://doi.org/10.1248/cpb.53.1065
3. N. Soni, V.K. Lal, S. Agrawal, S. Kadam and H. Verma, *Int. J. Pharm. Sci. Res.*, **8**, 2407 (2012).
4. D.A. Baranenko, M.K. Kurbonova, W. Lu and J. Jing, in eds.: J. Akhtar, M. Sarwat and F. Bashir, Plants of Chinese Origin for the Management of Neurodegenerative Diseases in the Elderly, In: Medicinal Plants for the Management of Neurodegenerative Diseases, CRC Press, edn 1, pp. 64-75 (2024).
5. A.A. Farooqi, G. Butt, S.A. El-Zahaby, R. Attar, U.Y. Sabitaliyevich, J.J. Jovic, K.-F. Tang, H. Naureen and B. Xu, *Pharmacol. Res.*, **160**, 105188 (2020); https://doi.org/10.1016/j.phrs.2020.105188
6. J. Hardy and D.J. Selkoe, *Science*, **297**, 353 (2002); https://doi.org/10.1126/science.1072994
7. D.D. Perrin, B. Dempsey and E.P. Serjeant, pK_a Prediction for Organic Acids and Bases, Chapman and Hall: London, vol. 1 (1981).
8. B. Alberts, A. Johnson, J. Lewis, M. Raff, K. Roberts and P. Walter, Molecular Biology of the Cell, Garland Science, New York, edn 4 (2002).
9. D.L. Nelson, A.L. Lehninger and M.M. Cox, Lehninger Principles of Biochemistry, Macmillan (2008).
10. C.P. Miller and E. Peter Stang, *Mol. Pharmacol.*, **90**, 713 (2022); https://doi.org/10.1124/mol.121.120246
11. S. Sharma, B. Nehru and A. Saini, *Neurochem. Int.*, **108**, 481 (2017); https://doi.org/10.1016/j.neuint.2017.06.011
12. S. Sharma and V. Bhatia, *Curr. Pharm. Des.*, **27**, 2848 (2021); https://doi.org/10.2174/1381612826666200928161721
13. M.J. Frisch, G.W. Trucks, H.B. Schlegel, G.E. Scuseria, M.A. Robb, J.R. Cheeseman, G. Scalmani, V. Barone, B. Mennucci, G.A. Petersson, H. Nakatsuji, M. Caricato, X. Li, H.P. Hratchian, A.F. Izmaylov, J. Bloino, G. Zheng, J.L. Sonnenberg, M. Hada, M. Ehara, K. Toyota, R. Fukuda, J. Hasegawa, M. Ishida, T. Nakajima, Y. Honda, O. Kitao, H. Nakai, T. Vreven, J.A. Montgomery Jr., J.E. Peralta, F. Ogliaro, J.J. Heyd, M. Bearpark, E. Brothers, K.N. Kudin, V.N. Staroverov, R. Kobayashi, J. Normand, K. Raghavachari, A. Rendell, J.C. Burant, S. S. Iyengar, M. Cossi, J. Tomasi, N. Rega, J. M. Millam, M. Klene, J. E. Knox, J.B. Cross, V. Bakken, C. Adamo, J. Jaramillo, R. Gomperts, R. E. Stratmann, O. Yazyev, A.J. Austin, R. Cammi, C. Pomelli, J.W. Ochterski, R.L. Martin, K. Morokuma, V.G. Zakrzewski, G.A. Voth, P. Salvador, J.J. Dannenberg, S. Dapprich, A.D. Daniels, Ö. Farkas, J.B. Foresman, J.V. Ortiz, J. Cioslowski and D. J. Fox, Gaussian 09, Revision B.01, Gaussian Inc. Wallingford, CT (2009).
14. R. Dennington, T. Keith and J. Millam, Gauss View, Version 5. Semichem Inc., Shawnee Mission (2009).

15. M.H. Jamróz, *Biomol.*, **114**, 220 (2013).
16. F. Cuenú, N. Muñoz-Patiño, J.E. Torres, R. Abonia, R.A. Toscano and J. Cobo, *J. Mol. Struct.*, **1148**, 557 (2017); https://doi.org/10.1016/j.molstruc.2017.07.038
17. T. Lu and F. Chen, *J. Comput. Chem.*, **33**, 580 (2012); https://doi.org/10.1002/jcc.22885
18. W. Humphrey, A. Dalke and K. Schulten, *J. Mol. Graph.*, **14**, 33 (1996); https://doi.org/10.1016/0263-7855(96)00018-5
19. A.E. Reed, L.A. Curtiss and F. Weinhold, *Chem. Rev.*, **88**, 899 (1988); https://doi.org/10.1021/cr00088a005
20. A. Daina, O. Michielin and V. Zoete, *Sci. Rep.*, **7**, 42717 (2017); https://doi.org/10.1038/srep42717
21. D.A. Filimonov, A.A. Lagunin, T.A. Gloriozova, D.S. Druzhilovskii, A.V. Rudik, P.V. Pogodin and V.V. Poroikov, *Chem. Heterocycl. Compd.*, **50**, 444 (2014); https://doi.org/10.1007/s10593-014-1496-1
22. R.A. Laskowski, M.W. MacArthur, D.S. Moss and J.M. Thornton, *J. Appl. Cryst.*, **26**, 283 (1993); https://doi.org/10.1107/S0021889892009944
23. R. Huey, G.M. Morris and S. Forli, Using AutoDock 4 and AutoDock Vina with AutoDockTools: A Tutorial, The Scripps Research Institute Molecular Graphics Laboratory, California, USA (2012).
24. D. Biovia, H. Berman, J. Westbrook, Z. Feng, G. Gilliland, T. Bhat and T.J.T.J.o.C.P. Richmond, Dassault Systèmes BIOVIA, Discovery Studio Visualizer, v. 17.2, San Diego: Dassault Systèmes, 2016, 10 (2000).
25. P. Banerjee, E. Kemmler, M. Dunkel and R. Preissner, *Nucleic Acids Res.*, **52(W1)**, W513 (2024); https://doi.org/10.1093/nar/gkae303
26. A.E. Blanchard, D. Bhowmik, Z. Fox, J. Gounley, J. Glaser, B.S. Akpa and S. Irle, *J. Cheminform.*, **15**, 59 (2023); https://doi.org/10.1186/s13321-023-00719-7
27. P. Schneider, W.P. Walters, A.T. Plowright, N. Sieroka, J. Listgarten, R.A. Goodnow Jr., J. Fisher, J.M. Jansen, J.S. Duca, T.S. Rush, M. Zentgraf, J.E. Hill, E. Krutoholow, M. Kohler, J. Blaney, K. Funatsu, C. Luebkemann and G. Schneider, *Nat. Rev. Drug Discov.*, **19**, 353 (2020); https://doi.org/10.1038/s41573-019-0050-3
28. S. Scheiner, *Phys. Chem. Chem. Phys.*, **13**, 13860 (2011); https://doi.org/10.1039/c1cp20427k
29. G.-J. Linker, P.T. van Duijnen and R. Broer, *J. Phys. Chem. A*, **124**, 1306 (2020); https://doi.org/10.1021/acs.jpca.9b10248
30. A. Orlando, F. Franceschini, C. Muscas, S. Pidkova, M. Bartoli, M. Rovere and A. Tagliaferro, *Chemosensors*, **9**, 262 (2021); https://doi.org/10.3390/chemosensors9090262
31. S. Zhang, Y. Qi, S.P.H. Tan, R. Bi and M. Olivo, *Biosensors*, **13**, 557 (2023); https://doi.org/10.3390/bios13050557
32. I.M. Alecu, J. Zheng, Y. Zhao and D.G. Truhlar, *J. Chem. Theory Comput.*, **6**, 2872 (2010); https://doi.org/10.1021/ct100326h
33. G. Bharathy, J.C. Prasana, V.S.J. Reeda, M. Prasath and A. Manikandan, *Chem. Phys. Impact*, **8**, 100558 (2024); https://doi.org/10.1016/j.chphi.2024.100558
34. P.S. Kalsi, Spectroscopy of Organic Compounds, New Age International, New Delhi, India (2007).
35. A. Kumar, M. Khandelwal, S.K. Gupta, V. Kumar and R. Rani, in eds.: G. Misra, Fourier Transform Infrared Spectroscopy: Data Interpretation and Applications in Structure Elucidation and Analysis of Small Molecules and Nanostructures; In: Data Processing Handbook for Complex Biological Data Sources, Academic Press, Chap. 6, pp. 77-96 (2019).
36. S. Yadav, S. Banik and M.D. Prasad, *Phys. Chem. Chem. Phys.*, **23**, 9176 (2021); https://doi.org/10.1039/D0CP01157F
37. D. Michalska, D.C. Bieñko, A.J. Abkowicz-Bieñko and Z. Latajka, *J. Phys. Chem.*, **100**, 17786 (1996); https://doi.org/10.1021/jp961376v
38. D. Kennepohl, S. Farmer and W. Reusch, Infrared Spectra of Some Common Functional Groups, LibreTexts: Chemistry (2020).
39. K. Hemachandran, P. Anbusrinivasan, S. Ramalingam, R. Aarthi and C.K. Nithya, *Heliyon*, **5**, e02788 (2019); https://doi.org/10.1016/j.heliyon.2019.e02788
40. B.F. Rizwana, J.C. Prasana and S. Muthu, *Int. J. Mater. Sci.*, **12**, 196 (2017).
41. K. Fukui, *Science*, **218**, 747 (1982); https://doi.org/10.1126/science.218.4574.747
42. G. Klopman, *J. Am. Chem. Soc.*, **90**, 223 (1968); https://doi.org/10.1021/ja01004a002
43. V.K. Rastogi, M.A. Palafox, L. Mittal, N. Peica, W. Kiefer, K. Lang and S.P. Ojha, *J. Raman Spectrosc.*, **38**, 1227 (2007); https://doi.org/10.1002/jrs.1725
44. R.G. Pearson, *J. Chem. Sci.*, **117**, 369 (2005); https://doi.org/10.1007/BF02708340
45. M. Miar, A. Shiroudi, K. Pourshamsian, A.R. Oliaey and F. Hatamjafari, *J. Chem. Res.*, **45**, 147 (2021); https://doi.org/10.1177/1747519820932091
46. P. Manjusha, J.C. Prasana, S. Muthu and B.F. Rizwana, *Chem. Data Coll.*, **20**, 100191 (2019); https://doi.org/10.1016/j.cdc.2019.100191
47. R. Rijal, M. Sah and H.P. Lamichhane, *Heliyon*, **9**, e14801 (2023); https://doi.org/10.1016/j.heliyon.2023.e14801
48. R.G. Parr, L.V. Szentpály and S. Liu, *J. Am. Chem. Soc.*, **121**, 1922 (1999); https://doi.org/10.1021/ja983494x
49. S.R. Gadre, C.H. Suresh and N. Mohan, *Molecules*, **26**, 3289 (2021); https://doi.org/10.3390/molecules26113289
50. K. Vedhapriya, G. Balaji, S. Sakthivel, S. Javed, M. Thirunavukkarasu and S. Muthu, *Chem. Phys. Impact*, **7**, 100262 (2023); https://doi.org/10.1016/j.chphi.2023.100262
51. B. Gopia and V. Vijayakumar, *RSC Adv.*, **14**, 13218 (2024); https://doi.org/10.1039/D4RA02151G
52. D.E. Arthur and A. Uzairu, *J. King Saud Univ. Sci.*, **31**, 1151 (2019); https://doi.org/10.1016/j.jksus.2019.01.011
53. J.D.D. Tarika, X.D.D. Dexlin, S. Madhankumar, D.D. Jayanthi and T.J. Beaula, *Spectrochim. Acta A Mol. Biomol. Spectrosc.*, **259**, 119907 (2021); https://doi.org/10.1016/j.saa.2021.119907
54. S.N. Steinmann, Y. Mo and C. Corminboeuf, *Phys. Chem. Chem. Phys.*, **13**, 20584 (2011); https://doi.org/10.1039/c1cp21055f
55. E.R. Johnson, S. Keinan, P. Mori-Sánchez, J. Contreras-García, A.J. Cohen and W. Yang, *J. Am. Chem. Soc.*, **132**, 6498 (2010); https://doi.org/10.1021/ja100936w
56. M. Thirunavukkarasu, P. Prabakaran, A. Saral, S. Kadaikunnan, N.S. Alharbi, A.S. Kazachenko and S. Muthu, *J. Mol. Liq.*, **380**, 121714 (2023); https://doi.org/10.1016/j.molliq.2023.121714
57. K. Rayene, D. Imane, B. Abdelaziz, N. Leila, M. Fatiha, G. Abdelkrim, G. Bouzid, L. Ismahan, H. Brahim and O. Rabah, *J. Mol. Struct.*, **1249**, 131565 (2022); https://doi.org/10.1016/j.molstruc.2021.131565
58. E. Eunice, J.C. Prasana, S. Muthu and A. Anuradha, *Polycycl. Aromat. Compd.*, **43**, 5747 (2023); https://doi.org/10.1080/10406638.2022.2107688
59. R.C. Wade and P.J. Goodford, *Prog. Clin. Biol. Res.*, **289**, 433 (1989).
60. F. Weinhold and C.R. Landis, *Chem. Educ. Res. Pract.*, **2**, 91 (2001); https://doi.org/10.1039/B1RP90011K
61. J. Cummings, Y. Zhou, G. Lee, K. Zhong, J. Fonseca and F. Cheng, *Alzheimers Dement.*, **10**, e12465 (2024); https://doi.org/10.1002/trc2.12465
62. S. Muthu and J. Uma Maheswari, *Spectrochim. Acta A Mol. Biomol. Spectrosc.*, **92**, 154 (2012); https://doi.org/10.1016/j.saa.2012.02.056
63. R.S. Mulliken, *J. Chem. Phys.*, **23**, 1833 (1955); https://doi.org/10.1063/1.1740588
64. S. Govindarajan and P.B. Nagabalasubramanian, *J. Adv. Sci. Eng.*, **2**, 75 (2015).
65. G. Venkatesh, M. Govindaraju, C. Kamal, P. Vennila and S.A.V.A. Kaya, *RSC Adv.*, **7**, 1401 (2017); https://doi.org/10.1039/C6RA25535C
66. A.L. Fussell, A. Isomaki and C.J. Strachan, *Am. Pharm. Rev.*, **16**, 54 (2013).
67. E. Eunice, J.C. Prasana, S. Kadaikunnan, N.S. Alharbi and S. Muthu, *J. Mol. Struct.*, **1319**, 139354 (2025); https://doi.org/10.1016/j.molstruc.2024.139354

68. A.K. Pandey, K.K. Pandey, D.D. Dubey, V. Singh and A. Dwivedi, *J. Mol. Liq.*, **420**, 126839 (2025); https://doi.org/10.1016/j.molliq.2024.126839
69. V. Parodi, E. Jacchetti, R. Osellame, G. Cerullo, D. Polli and M.T. Raimondi, *Front. Bioeng. Biotechnol.*, **8**, 585363 (2020); https://doi.org/10.3389/fbioe.2020.585363
70. R. Kato, W. Zeng, V.B. Siramshetty, J. Williams, M. Kabir, N. Hagen, E.C. Padilha, A.Q. Wang, E.A. Mathé, X. Xu and P. Shah, *Front. Pharmacol.*, **14**, 1291246 (2023); https://doi.org/10.3389/fphar.2023.1291246
71. A. Daina and V. Zoete, *ChemMedChem*, **11**, 1117 (2016); https://doi.org/10.1002/cmdc.201600182
72. H. Pajouhesh and G.R. Lenz, *NeuroRx*, **2**, 541 (2005); https://doi.org/10.1602/neurorx.2.4.541
73. S. Shityakov, W. Neuhaus, T. Dandekar and C. Förster, *Int. J. Comput. Biol. Drug Des.*, **6**, 146 (2013); https://doi.org/10.1504/IJCBDD.2013.052195
74. M. Elmeliegy, M. Vourvahis, C. Guo and D.D. Wang, *Clin. Pharmacokinet.*, **59**, 699 (2020); https://doi.org/10.1007/s40262-020-00867-1
75. G. Miebs, A. Mielniczuk, M. Kadziński and R.A. Bachorz, *Appl. Sci.*, **14**, 9966 (2024); https://doi.org/10.3390/app14219966
76. V. Ivanovic, M. Ranèic, B. Arsic and A. Pavlovic, *Chemia Naissensis*, **3**, 171 (2020).
77. A. Bhargava, P. Shrivastava and A. Tilwari, *Future J. Pharm. Sci.*, **7**, 1 (2021); https://doi.org/10.1186/s43094-020-00150-x
78. J. Van Meerloo, G.J.L. Kaspers and J. Cloos, *Methods Mol. Biol*., **731**, 237 (2011); https://doi.org/10.1007/978-1-61779-080-5_20
79. L. Florento, R. Matias, E. Tuano, K. Santiago, F. Cruz and A. Tuazon, *Int. J. Biomed. Sci.*, **8**, 76 (2012); https://doi.org/10.59566/IJBS.2012.8076
80. H.M. Berman, J. Westbrook, Z. Feng, G. Gilliland, T.N. Bhat, H. Weissig, I.N. Shindyalov, P.E. Bourne, *Nucleic Acids Res.*, **28**, 235 (2000); https://doi.org/10.1093/nar/28.1.235
81. R.W. Hooft, C. Sander and G. Vriend, *Bioinformatics*, **13**, 425 (1997); https://doi.org/10.1093/bioinformatics/13.4.425
82. D.S. Spassov, *Int. J. Mol. Sci.*, **25**, 7124 (2024); https://doi.org/10.3390/ijms25137124
83. A. Sethi, K. Joshi, K. Sasikala and M. Alvala, Molecular Docking in Modern Drug Discovery: Principles and Recent Applications, In: Drug Discovery Development-New Advances, IntechOpen, pp. 1-21 (2019).
84. L.G. Ferreira, R.N. Dos Santos, G. Oliva and A.D. Andricopulo, *Molecules*, **20**, 13384 (2015); https://doi.org/10.3390/molecules200713384
85. U. Neumann, M. Ufer, L.H. Jacobson, M.-L. Rouzade Dominguez, G. Huledal, C. Kolly, R.M. Lüönd, R. Machauer, S.J. Veenstra, K. Hurth, H. Rueeger, M. Tintelnot-Blomley, M. Staufenbiel, D.R. Shimshek, L. Perrot, W. Frieauff, V. Dubost, H. Schiller, B. Vogg, K. Beltz, A. Avrameas, S. Kretz, N. Pezous, J.-M. Rondeau, N. Beckmann, A. Hartmann, S. Vormfelde, O.J. David, B. Galli, R. Ramos, A. Graf and C. Lopez-Lopez, *EMBO Mol. Med.*, **10**, e9316 (2018); https://doi.org/10.15252/emmm.201809316
86. J.-P. Colletier, D. Fournier, H.M. Greenblatt, J. Stojan, J.L. Sussman, G. Zaccai, I. Silman and M. Weik, *EMBO J.*, **25**, 2746 (2006); https://doi.org/10.1038/sj.emboj.7601175
87. National Center for Biotechnology Information. PubChem Compound Summary for CID 9651, Galantamine. Accessed 18 November, 2024; https://pubchem.ncbi.nlm.nih.gov/compound/Galantamine
88. R.T. Bhagat, S.R. Butle, D.S. Khobragade, S.B. Wankhede, C.C. Prasad, D.S. Mahure and A.V. Armarkar, *J. Pharm. Res. Int.*, **33**, 46 (2021); https://doi.org/10.9734/jpri/2021/v33i30B31639